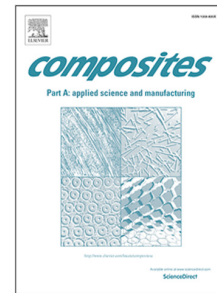# Journal Pre-proof

Rate-dependent 3D forming simulation of thermoplastic composite materials using visco-hyperelastic material modeling and 3D hexahedral solid-shell elements

Johannes Mitsch, Bastian Schäfer, Luise Kärger

Please cite this article as: J. Mitsch, B. Schäfer and L. Kärger, Rate-dependent 3D forming simulation of thermoplastic composite materials using visco-hyperelastic material modeling and 3D hexahedral solid-shell elements. *Composites Part A* (2025), doi: https://doi.org/10.1016/j.compositesa.2025.109306.

Rate-dependent 3D forming simulation of thermoplastic composite materials using visco-hyperelastic material modeling and 3D hexahedral solid-shell elements

Highlights

Rate-dependent 3D forming simulation of thermoplastic composite materials using visco-hyperelastic material modeling and 3D hexahedral solid-shell elements

Johannes Mitsch, Bastian Schäfer, Luise Kärger

- Enhanced hexahedral solid-shell element for the 3D thermoforming simulation of thermoplastic composite materials

- Visco-hyperelastic 3D material modeling for the solid-shell element formulation, enabling rate-dependent 3D forming simulation of thermoplastic composite materials

- Demonstrated transferability of material datasets from an established 2D approach to accelerate material parameter identification and characterization for the 3D solid-shell element

- Numerical validation of the solid-shell element formulation through comparisons with an experimentally validated 2D approach

- Prediction of local thickness changes during the forming process

Rate-dependent 3D forming simulation of thermoplastic composite materials using visco-hyperelastic material modeling and 3D hexahedral solid-shell elements

Johannes Mitsch[a,*], Bastian Schäfer[a], Luise Kärger[a,**]

[a]*Lightweight Engineering, Institute of Vehicle System Technology (FAST), Karlsruhe Institute of Technology (KIT), Karlsruhe, 76131, Germany*

Abstract

The Finite Element Method is a widely applied approach for predicting manufacturing effects in the thermo-forming process of fiber-reinforced composite materials. The majority of macroscopic simulation approaches are based on shell elements with two-dimensional (2D) stress states and provide efficient predictions of the forming process of composite materials. However, they lack the ability to capture through-thickness behavior due to their dimensional limitations. The present study proposes a three-dimensional (3D) solid-shell element formulation that incorporates rate-dependent material modeling thus enabling the simulation of the thermoforming process of thermoplastic composites. The solid-shell element formulation provides a locking-free formulation, an hourglass stabilization technique to prevent zero-energy modes, a reduced integration scheme, and the consideration of a rate-dependent material behavior. An analysis of the correspondence between the material parameters of the 3D solid-shell element and an experimentally validated 2D approach indicates that the 2D approach can effectively be employed to characterize in-plane and bending material parameters for the 3D solid-shell element formulation, streamlining and accelerating its material parameter identification process. The parameterization of the nonlinear compaction behavior of the solid-shell element exhibits a strong correlation with experimental results from existing literature. Finally, the solid-shell element is utilized to simulate the thermoforming process of a thermoplastic tape, yielding results that closely match those obtained from a 2D approach. The predicted thickness distribution, determined by the new 3D solid-shell, agrees well with the expected results, confirming the validity and practical potential of the proposed approach.

Keywords: Finite Element Analysis, Process simulation, Thermoforming, Composite Forming Simulation, Solid-shell

1. Introduction

1.1. Motivation

The quality of continuous fiber-reinforced thermoplastic (CoFRTP) components is significantly influenced by the manufacturing process and the process configuration. The significance of process parameters such

---

as temperature [1, 2], grippers [3, 4, 5], and initial fiber orientation [6, 7] on the final part geometry is well documented. However, the experimental optimization of these parameters can be time-consuming and costly. Therefore, the Finite Element Method (FEM) has become an essential tool for designing and optimizing the forming processes of CoFRTP, as it enables a virtual optimization of the manufacturing process [8, 9].

Over the past two decades, significant progress has been made in the development of simulation tools for the thermoforming of continuous fiber-reinforced plastics [10, 11, 12, 13]. Despite these advancements, the majority of macroscopic simulation approaches rely on shell elements with 2D stress states [9]. Given the characteristic thin-walled geometry of CoFRTP sheets, these models have been proven efficient in capturing in-plane membrane behavior, out-of-plane bending, and inter-ply interactions. Consequently, they possess the capability to accurately predict the geometry of the final part, fiber orientation and wrinkling phenomena [11]. However, these elements inherently cannot model the through-thickness behavior of CoFRTPs, e.g., out-of-plane compaction or through-thickness thermal gradients. This constraint is attributed to the absence of the required degrees of freedom to represent through-thickness deformation and through-thickness temperature distributions. This limitation becomes critical when predicting final part thickness, local fiber volume content, press forces or locally varying material properties due to heating or contact conditions. These parameters are essential for optimizing the forming process and are crucial for subsequent simulation steps, e.g. the warpage simulation [14]. To enable material modeling in thickness direction, 3D finite elements are required [15]. However, standard 3D finite elements are vulnerable to numerical locking phenomena and therefore are not suitable for the simulation of the forming process of CoFRTP. Consequently, the development of a specialized 3D finite element formulation is necessary to enable the simulation of the forming process of CoFRTPs.

1.2. Related work

1.2.1. Forming simulation of CoFRTPs using two-dimensional element approaches

CoFRTPs exhibit high tensile stiffness along the fiber direction, due to the presence of quasi-inextensible fibers. In contrast, the matrix material adds strong time- and temperature-dependent behavior. Despite their high tensile stiffness, CoFRTPs show relatively low resistance to bending deformation. This is attributed to the low transverse shear stiffness in pre-impregnated textiles resulting in dominant relative motion between fibers during bending [16]. Therefore, constitutive modelling of the membrane and the bending response in a decoupled manner is necessary to accurately capture the forming behavior of CoFRTPs and predict the wrinkling behavior during forming [17, 18, 19, 20].

Two-dimensional shell approaches achieve a membrane-bending decomposition by, for example, employing superimposed membrane and shell elements or specific out-of-plane integration schemes [20, 21, 22, 23]. Initially, bending behavior was either neglected from consideration [24, 25] or modeled purely elastic [20, 26]. However, Dörr et al. [21, 27] and Alshahrani and Hojjati [28] proved that the rate-dependent modelling of the bending behavior is crucial for the accurate prediction of the wrinkling behavior in the thermoforming process of CoFRTPs. Therefore, the rate-dependent nature of the material response is typically captured using viscoelastic models such as the Voigt-Kelvin model [20, 21] or a generalized Maxwell approach [26, 27]. Thermoforming of CoFRTPs is typically performed at elevated temperatures well above the crystallization temperature of the matrix material. During forming, convective cooling of the blank and contact with the colder mold can lower the temperature, significantly affecting the material behavior [29, 30] and making

the prediction of crystallization kinetics essential in thermoforming simulations [31]. Recent studies have implemented coupled thermomechanical approaches to capture temperature-dependent shear and bending behavior [26] and phase transitions between fluid and solid states within the thermoplastic material [22]. In particular, advances in thermomechanical modeling have emphasized the need for accurate prediction of temperature distribution through the thickness during thermoforming [32]. These works are based on the Alternate Direction Implicit (ADI) formulation [33], which effectively decomposes the thermal problem into a two-dimensional in-plane component and a one-dimensional through-thickness component. This approach enables 3D-like thermal modeling while maintaining computational efficiency through 2D mechanical shell elements making this approach particularly suitable for multi-layer simulation models [32]. Building upon a fully three-dimensional framework for through-thickness mechanical and thermal behavior, the fully coupled thermo-kinetic visco-hyperelastic constitutive model proposed by Bigot et al. [34] at the coupon scale could be extended in future work to simulate industrial-scale thermoforming processes of CoFRTPs.

1.2.2. 3D solid-shell elements

Despite significant advancements in thermoforming simulations for CoFRTPs, there remains a lack of simulation approaches capable of simultaneously capturing the compaction behavior of the material and predicting final part geometry. A finite element class which show promising results for the simulation of sheet metal forming are so-called solid-shell elements [35, 36, 37]. Solid-shell elements are a class of 3D finite elements that capture the behavior of thin-walled structures while avoiding the numerical locking issues (especially during bending deformation) associated with traditional solid elements. Unlike conventional shell elements, solid-shell elements allow for full 3D material modeling capabilities and therefore are a promising candidate to predict the compaction behavior within the simulation of the forming process for CoFRTPs. However, it is essential to note that these elements require a membrane-bending decomposition in order to accurately predict the wrinkling behavior during the forming process.

A large variety of solid-shell elements have been developed in the past, which are compared in detail by, e.g., Rah et al. [38], Schwarze and Reese [39, 40], Mostafa [41]. The primary distinction among the various implementations of solid-shell elements pertains to their methods to avoid numerical locking based on the integration scheme, the number of collocation points for the *Assumed Natural Strain* (ANS)-method, and the number of *Enhanced Assumed Strain* (EAS) degrees of freedom (DOF). First implementations of solid-shell elements for implicit time-integration were initially proposed for the simulation of metal forming processes [42, 43, 44]. The formulation was later modified for explicit time-integration [45]. First proposals of solid-shell elements with a single integration point and three EAS-DOF were presented by Reese et al. [46] and Reese [47] which was later extended to variable number of integration points in thickness direction [48, 49]. As reduced-integrated element formulations are numerically more efficient and less vulnerable to numerical locking phenomena, they are more suitable for the simulation of the forming process of CoFRTPs but need material-specific hourglass stabilization techniques.

1.2.3. Simulation approaches for the forming simulation of CoFRTPs employing 3D element formulations

An 8-node solid-shell element for the forming simulation of woven thermoplastic composites was proposed by Chen et al. [50, 51]. The initial formulation demonstrates the capability to produce plausible results for shear angle distribution during the forming of complex geometries such as hemispherical and box-shaped parts [50]. In a follow-up study, the formulation was extended to include a viscoelastic material model and to

3

investigate inter-ply slippage phenomena during the forming process [51]. However, no methods to consider a membrane-bending decomposition or to prevent numerical locking phenomena were proposed.

Xiong et al. [52, 53] proposed a solid-shell element based on a 6-node prismatic element to model the consolidation of thermoplastic composite prepregs. The compaction behavior is incorporated through the implementation of an additional node in the element center, thereby enabling the prediction of pinching stresses. The solid-shell element utilizes a viscoelastic model based on a generalized Maxwell approach. The model incorporates an intimate contact model to describe the void reduction with time, pressure, and temperature. The model is able to accurately predict the compaction behavior within a thermoforming simulation of a double-dome geometry. The implementation necessitates a global DOF in contrast to an internal EAS-DOF, thereby constraining the implementation to specific solvers.

Dia et al. [54] proposed a nine-node hexahedral solid-shell element based on the geometry of a standard brick element. The formulation includes an additional node at the center of the element, equipped with a single degree of freedom in the thickness direction, enabling full 3D material modeling and improving the prediction of pinching stresses. To mitigate transverse shear locking, the element employs the ANS-method using a 4-node approach. The central degree of freedom is conceptually analogous to the enhancements introduced by the EAS method but offers enhanced accuracy in capturing through-thickness stress distributions compared to EAS-DOFs. This is because the EAS degrees of freedom do not significantly contribute to through-thickness stress prediction and are insufficient for accurately satisfying Neumann boundary conditions under transverse pressure loading, whereas the central node in Dia et al. [54] enables direct representation of these stress components. No methods involving a membrane-bending decomposition were proposed.

Poppe et al. [55, 56] implemented a built-in prismatic continuum shell element (SC6R) in combination with a user-defined element within Abaqus/Explicit (VUEL) to simulate the nonlinear compaction and simultaneous infiltration processes of wet compression molding. In order to capture the fabric's low bending stiffness, the model reduces the transverse shear stiffness rather than employing a full decoupling of the membrane and bending behavior. While this approach provides a reasonable approximation of the out-of-plane mechanical response, it inherently assumes an isotropic bending behavior with constant bending stiffness.

The solid-shell element formulation employed in this work is based on the Q1STs element formulation originally proposed by Schwarze and Reese [39, 40], which features a reduced in-plane integration scheme, a four-point ANS-method, and a single EAS-DOF. This formulation was later adapted for explicit time integration by Pagani et al. [36], and its application was successfully demonstrated for the structural simulation of consolidated CoFRTPs [57, 58]. However, its use in simulating the forming process of CoFRTPs was limited due to the absence of a membrane-bending decomposition [59]. To address this limitation, a further development of the Q1STs-based solid-shell element was introduced by Schäfer et al. [60, 61] for the simulation of textile fabric forming processes. This enhanced formulation retains the key features while additionally enabling a membrane-bending decomposition. As a result, it allows for accurate predictions of wrinkling and realistic compaction behavior of textile fabrics during forming. However, the formulation currently does not support rate-dependent material models, thereby preventing its direct applicability to the thermoforming simulation of CoFRTPs.

The authors of the present work have previously proposed a 3D solid-shell element formulation for the

4

126 thermoforming simulation of CoFRTPs [62, 63]. This formulation builds upon the Q1STs element [39, 40]
127 and incorporates the modifications introduced by Schäfer et al. [60, 61] to enable a membrane-bending
128 decomposition. It was shown that the proposed formulation conceptually captures rate-dependent material
129 behavior in numerical coupon tests using generic material parameters [62]. Building on this, a parameter
130 study to assess the influence of material properties on the global deformation behavior during thermoforming
131 simulation was conducted [63]. The findings indicated that parameters governing rate-dependency and
132 bending behavior in the fiber direction exert a substantial influence on the global deformation behavior
133 and must therefore be characterized precisely, whereas transverse shear properties have a minor impact on
134 deformation and can be approximated within a reasonable order of magnitude to ensure numerical stability.
135 Neither study included a comparison of the solid-shell formulation with experiments or an experimentally
136 validated reference model to validate the global deformation behavior of the solid-shell element formulation.
137 Also an evaluation of the resulting thickness distribution of the final part geometry was not performed.

1.3. Scope of this work and novel aspects

139 The objective of this study is to develop a 3D finite element formulation based on an 8-node hexahedral
140 solid-shell element for the isothermal viscoelastic thermoforming simulation for CoFRTPs. The finite element
141 is based on the Q1STs element formulation that was proposed by Schwarze and Reese [39, 40] and was
142 further developed by Schäfer et al. [60, 61] to enable the simulation of the forming process of dry textile
143 fabrics. The element formulation is implemented as a user-defined element VUEL for the commercial finite
144 element software Abaqus. This work enhances the finite element formulation by newly incorporating a rate-
145 dependent material behavior to predict the global deformation behavior during the thermoforming process for
146 CoFRTPs. Additionally, a nonlinear compaction model is proposed and parameterized using experimental
147 data from literature. To reduce the effort associated with material characterization for the solid-shell element,
148 a new method for transferring of material properties from a 2D approach is investigated through a series
149 of coupon-level simulations. The proposed 3D solid-shell element is validated by comparing the results of
150 a single-layer CoFRTP thermoforming simulation against those obtained using an experimentally validated
151 2D approach, as a reference model. Finally, the thickness distribution of the final part geometry is evaluated
152 to demonstrate the solid-shell element's capability to predict local thickness variations during the forming
153 process.

2. Material modelling

2.1. Visco-hyperelastic membrane and bending modeling

156 To model the rate-dependent material behavior of the thermoplastic CoFRTPs, a visco-hyperelastic
157 material model is employed. The visco-hyperelastic material model is applied in a decoupled manner for the
158 in-plane membrane behavior and the bending behavior of the CoFRTPs. The membrane behavior is modeled
159 using the Voigt-Kelvin approach and the *Ideal Fiber Reinforced Material* (IFRM) model [64, 65]. The model
160 ensures the quasi-inextensibility of the CoFRTPs in fiber direction through elevated elastic stiffnesses in
161 that direction which is a common assumption for forming simulation of composites [19, 21]. The bending
162 behavior is modeled using the Voigt-Kelvin approach.

5

2.1.1. Voigt-Kelvin model

The Voigt-Kelvin model can be described as a parallel connection of a spring and a damper, wherein the spring represents the elastic behavior and the damper represents the viscous material response. Accordingly, the second Piola-Kirchhoff stress tensor $\boldsymbol{S}^{\text{2PK}}$ is calculated by [66]

$$\boldsymbol{S}^{\text{2PK}} = \boldsymbol{S}^{\text{2PK}}_{\text{elas}} + \boldsymbol{S}^{\text{2PK}}_{\text{visc}}, \tag{1}$$

comprising an elastic component $\boldsymbol{S}^{\text{2PK}}_{\text{elas}}$ and a viscous component $\boldsymbol{S}^{\text{2PK}}_{\text{visc}}$. The elastic stress component $\boldsymbol{S}^{\text{2PK}}_{\text{elas}}$ is connected to a strain energy $W = 1/2\ \boldsymbol{E} \cdot \mathbb{C}[\boldsymbol{E}]$ and can be calculated using the hyperelastic St. Venant-Kirchhoff model [67]

$$\boldsymbol{S}^{\text{2PK}}_{\text{elas}} = \mathbb{C}[\boldsymbol{E}], \tag{2}$$

where $\mathbb{C}$ represents the stiffness tensor, while $\boldsymbol{E}$ denotes the Green-Lagrange strain tensor. Due to the dominant in-plane characteristics of CoFRTPs, the stiffness tensor $\mathbb{C}$ is typically highly anisotropic, characterized by a high stiffness along the fiber direction and significantly lower stiffnesses in both the transverse and shear directions.

The viscous part of the Voigt-Kelvin approach (Equation (1)) is modeled utilizing an isotropic Newton model [68]

$$\boldsymbol{\sigma}_{\text{visc}} = \eta \boldsymbol{D}, \tag{3}$$

where the viscous Cauchy stress $\boldsymbol{\sigma}_{\text{visc}}$ is calculated using the viscosity η and the deformation rate tensor $\boldsymbol{D}$. In this work, the viscosity η (Equation (3)) is modelled using the Cross model, which defines the viscosity as a function of the scalar deformation rate $\dot{\gamma}$ [68]

$$\eta(\dot{\gamma}) = \frac{\eta_0 - \eta_\infty}{1 + m\dot{\gamma}^{(1-n)}}\eta_\infty. \tag{4}$$

In Equation (4), η_0 is the zero shear viscosity, η_∞ the infinite shear viscosity, and m and n are Cross model parameters. The deformation rate $\dot{\gamma}$ is the Frobenius norm of $\boldsymbol{D}$

$$\dot{\gamma} = \sqrt{2\boldsymbol{D} \cdot \boldsymbol{D}}. \tag{5}$$

Using the rate of the Green-Lagrange strain tensor $\dot{\boldsymbol{E}}$ [66], $\boldsymbol{D}$ can be calculated

$$\boldsymbol{D} = \boldsymbol{F}^{-\top}\dot{\boldsymbol{E}}\boldsymbol{F}^{-1}. \tag{6}$$

To evaluate Equation (1) in the initial configuration, the viscous Cauchy stress $\boldsymbol{\sigma}_{\text{visc}}$ is transformed to the second Piola-Kirchhoff stress tensor $\boldsymbol{S}^{\text{2PK}}_{\text{visc}}$ using the deformation gradient tensor $\boldsymbol{F}$ and its determinant $J = \det(\boldsymbol{F})$

$$\boldsymbol{S}^{\text{2PK}}_{\text{visc}} = J\boldsymbol{F}^{-1}\boldsymbol{\sigma}_{\text{visc}}\boldsymbol{F}^{-\top}. \tag{7}$$

Note, that the Voigt-Kelvin approach (Equation (1)) is a comparably simple model for the rate-dependent membrane and bending behavior of CoFRTPs. More sophisticated multi-mode formulations, such as generalized Maxwell models with Prony-series relaxation (e.g., [26, 27]), can represent a broader range of relaxation times and long-term viscous effects and can model the viscoelastic behavior more realistically. However, in

189 the present work, the Voigt-Kelvin approach is chosen for its simplicity and computational efficiency.

190 *2.2. Nonlinear compaction behavior*

191 The experimental investigations in the literature demonstrate that the compaction behavior of CoFRTPs
192 is nonlinear and follows an exponential progression for rising compaction displacements [53, 69]. To model
193 the nonlinear compaction behavior of CoFRTPs, the compaction stiffness C_{C} is modeled as an exponential
194 function of the compaction strain E_{33}. Therefore, the following approach is employed

$$C_{\mathrm{C}}\left(E_{33}\right) = a \cdot \exp\left(-c \cdot E_{33}\right),\tag{8}$$

195 where a and c are fitting parameters.

196 To identify the parameters a and c, the deformation is assumed purely compressive, i.e., without con-
197 sideration of Poisson's ratios. The deformation gradient $\boldsymbol{F}_{\mathrm{C}}$, which describes the deformation state, can be
198 expressed as

$$\boldsymbol{F}_{\mathrm{C}} = \begin{bmatrix} 1 & 0 & 0 \\ 0 & 1 & 0 \\ 0 & 0 & \lambda_z \end{bmatrix} \boldsymbol{e}_i \otimes \boldsymbol{e}_j \text{ with } \lambda_z = \frac{t - u_{\mathrm{C}}}{t}.\tag{9}$$

199 Here, $\lambda_z \in [0,1]$ describes the relative thickness deviation of the CoFRTP with the initial thickness t and
200 the compaction displacement u_{C}. The corresponding Green-Lagrange strain tensor $\boldsymbol{E}$ can be obtained by

$$\boldsymbol{E} = \frac{1}{2}\left(\boldsymbol{F}_{\mathrm{C}}^{\top}\boldsymbol{F}_{\mathrm{C}} - \boldsymbol{I}\right).\tag{10}$$

201 In a subsequent evaluation step, the experimentally measured compaction force R_{C} is used to calculate
202 the corresponding second Piola-Kirchhoff stress tensor $\boldsymbol{S}^{\mathrm{2PK}}$. For this the first Piola-Kirchhoff stress tensor
203 $\boldsymbol{S}^{\mathrm{1PK}}$ is computed using the initial cross-sectional area A and the measured compaction force R_{C}

$$\boldsymbol{S}^{\mathrm{1PK}} = \frac{R_{\mathrm{C}}}{A}\boldsymbol{e}_3 \otimes \boldsymbol{e}_3.\tag{11}$$

204 The second Piola-Kirchhoff stress tensor $\boldsymbol{S}^{\mathrm{2PK}}$ can be calculated using the deformation gradient $\boldsymbol{F}_{\mathrm{C}}$

$$\boldsymbol{S}^{\mathrm{2PK}} = \boldsymbol{F}_{\mathrm{C}}^{-1}\boldsymbol{S}^{\mathrm{1PK}}.\tag{12}$$

205 Finally, by combining the kinematic assumption (Equation (9)) with the kinematic identities (Equation (10),
206 Equation (11) and Equation (12)) and the constitutive model (Equation (2), Equation (8)), the fitting
207 parameters a and c can be determined.

3. Element formulations

209 *3.1. Two-dimensional approach*

210 *3.1.1. Implementation in Abaqus/Explicit using superimposed two-dimensional elements*

211 In this study, an experimentally validated methodology for macroscopic thermoforming simulation of
212 CoFRTPs using a 2D approach, utilizing a decomposition of membrane and bending behavior is employed

7

213 for comparison. The approach is implemented in the commercial finite element software Abaqus/Explicit
214 and is based on the work of Dörr et al. [21].

215 To decompose membrane and bending behavior, separate membrane and plate (bending) elements are
216 superimposed at shared nodes. This strategy allows for the independent computation of in-plane forces
217 $\boldsymbol{N}$ and bending moments $\boldsymbol{M}$ within the respective elements, enabling a decomposed and consistent rep-
218 resentation of in-plane membrane and out-of-plane bending material responses in a unified finite element
219 formulation. The membrane's behavior is described using membrane elements (M3D3) and a VUMAT
220 subroutine. The bending behavior is modeled using shell elements (S3) and a VUGENS subroutine which
221 computes the bending moments $\boldsymbol{M}$ from the incremental curvature tensors $\Delta\boldsymbol{\kappa}$ at the shell mid-face. The
222 material models for both the membrane and bending behavior are based on the Voigt-Kelvin approach from
223 Section 2.1.1.

3.1.2. Parameters of the 2D material model

225 As this work investigates the correspondence of material parameters using different element formulations,
226 a brief overview of the material parameters used in the 2D approach is provided in the following.

227 Two distinct elastic stiffness tensors, $\mathbb{C}^{2\mathrm{D,M}}$ and $\mathbb{C}^{2\mathrm{D,B}}$, are defined for the elastic membrane and bending
228 behavior. The elastic law for the membrane in 2D Voigt-notation reads (cf. Equation (2))

$$\underbrace{\begin{bmatrix} E_{\mathrm{F}}^{2\mathrm{D,M}} + E_{\mathrm{M}}^{2\mathrm{D,M}} & 0 & 0 \\ 0 & E_{\mathrm{M}}^{2\mathrm{D,M}} & 0 \\ 0 & 0 & G_{\mathrm{M}}^{2\mathrm{D,M}} \end{bmatrix}}_{\mathrel{\hat=}\,\mathbb{C}^{2\mathrm{D,M}}} \underbrace{\begin{bmatrix} E_{11}^{2\mathrm{D,M}} \\ E_{22}^{2\mathrm{D,M}} \\ 2E_{12}^{2\mathrm{D,M}} \end{bmatrix}}_{\mathrel{\hat=}\,\boldsymbol{E}^{2\mathrm{D,M}}} = \underbrace{\begin{bmatrix} S_{11}^{2\mathrm{D,M}} \\ S_{22}^{2\mathrm{D,M}} \\ S_{12}^{2\mathrm{D,M}} \end{bmatrix}}_{\mathrel{\hat=}\,\boldsymbol{S}_{\mathrm{elast}}^{2\mathrm{D,M}}}. \tag{13}$$

229 The Youngs Moduli $E_{\mathrm{F}}^{2\mathrm{D,M}}$ represent the stiffness in fiber direction. The modulus $E_{\mathrm{M}}^{2\mathrm{D,M}}$ describes the
230 isotropic stiffness of the matrix, which is typically several orders of magnitude lower than the stiffness along
231 the fiber direction. The in-plane Possion ratio $\nu_{12}^{2\mathrm{D,M}}$ is assumed to be negligible due to the high contrast
232 between the in-plane stiffnesses. Consequently, the in-plane shear modulus $G_{\mathrm{M}}^{2\mathrm{D,M}}$ can be calculated using

$$G_{\mathrm{M}}^{2\mathrm{D,M}} = \frac{E_{\mathrm{M}}^{2\mathrm{D,M}}}{2\left(1 + \nu_{12}^{2\mathrm{D,M}}\right)} = \frac{E_{\mathrm{M}}^{2\mathrm{D,M}}}{2}. \tag{14}$$

233 The elastic law for the bending in 2D Voigt-notation reads (cf. Equation (2))

$$\underbrace{\begin{bmatrix} C_{11}^{2\mathrm{D,B}} & 0 & 0 \\ 0 & C_{22}^{2\mathrm{D,B}} & 0 \\ 0 & 0 & C_{12}^{2\mathrm{D,B}} \end{bmatrix}}_{\mathrel{\hat=}\,\mathbb{C}^{2\mathrm{D,B}}} \underbrace{\begin{bmatrix} \varepsilon_{11}^{2\mathrm{D,B}} \\ \varepsilon_{22}^{2\mathrm{D,B}} \\ 2\varepsilon_{12}^{2\mathrm{D,B}} \end{bmatrix}}_{\mathrel{\hat=}\,\boldsymbol{\varepsilon}^{2\mathrm{D,B}}} = \underbrace{\begin{bmatrix} \sigma_{11}^{2\mathrm{D,B}} \\ \sigma_{22}^{2\mathrm{D,B}} \\ \sigma_{12}^{2\mathrm{D,B}} \end{bmatrix}}_{\mathrel{\hat=}\,\boldsymbol{\sigma}_{\mathrm{elast}}^{2\mathrm{D,B}}}. \tag{15}$$

234 The bending stiffnesses $C_{11}^{2\mathrm{D,B}}$ and $C_{22}^{2\mathrm{D,B}}$ describe the stiffnesses in fiber direction and perpendicular to
235 the fiber direction, respectively. The bending stiffness $C_{12}^{2\mathrm{D,B}}$ characterizes the bending resistance along the
236 direction diagonal to the material's principal axes. Note that the 2D approach uses infinitesimal strain
237 theory, as the strain tensor $\boldsymbol{\varepsilon}$ is approximated in the VUGENS subroutine [21].

238 The viscous behavior within the 2D approach follows an isotropic Newton model (Equation (3)) extended
239 by a Cross viscosity law (Equation (4)). The rate-dependent approach is applied separately for the membrane
240 and bending behavior. Therefore, the viscous material parameters η_0^{2D}, η_∞^{2D}, m^{2D}, and n^{2D} are required for
241 both the membrane and bending behavior.

3.2. Solid-Shell Element

3.2.1. Fundamental element formulation

244 The 3D hexahedral solid-shell element utilized in this study is based on the Q1STs element originally
245 proposed by Schwarze and Reese [39, 40] and was extended to an explicit formulation by Pagani et al. [36].
246 An exhaustive derivation of the element formulation can be found in the original publications. A concise
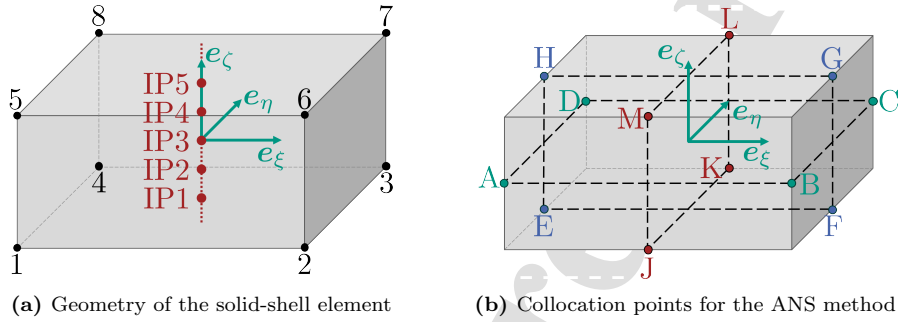247 overview of the major features of the solid-shell element used is given below.

(a) Geometry of the solid-shell element   **(b)** Collocation points for the ANS method

Figure 1: Isoparametric solid-shell element (based on [35, 39, 40])

248 The geometry of the used solid-shell element utilised is a standard 8-node hexahedral finite element
249 with only translational degrees of freedom, cf. Figure 1a. For the interpolation of the displacements within
250 the element, tri-linear shape functions are employed. These shape functions are defined in the natural
251 coordinates $\boldsymbol{\xi} \mathrel{\widehat{=}} (\xi, \eta, \zeta)^\top$ of the element [67]

$$N_I = \frac{1}{8}(1 + \xi\xi_I)(1 + \eta\eta_I)(1 + \zeta\zeta_I), \quad I = 1, \ldots, 8. \tag{16}$$

252 Here, $\boldsymbol{\xi}_I$ are the natural coordinates of the nodes of the element. In order to carry out the numerical
253 integration of the weak form, a reduced integration scheme is utilized in the in-plane direction, and a full
254 integration is employed in the thickness direction. The full integration in thickness direction is performed
255 using a standard Gauss-Legendre quadrature with a variable number of integration points. The integration
256 points are stacked in the middle plane of the element in thickness direction and their locations are given
257 by $\boldsymbol{\xi}^\star = \zeta^\star \boldsymbol{e}_\zeta$ (cf. Figure 1a). Note, that the natural coordinates of the integration points $\zeta^\star$ and the
258 corresponding weights for the numerical integration depend on the selected number of integration points.
259 In order to prevent numerical locking phenomena, a variety of computational techniques are employed,
260 modifying the strain $\boldsymbol{E}$ in the solid-shell element. The strain tensor $\boldsymbol{E}$ in natural coordinates $\boldsymbol{\xi}$ reads

$$\boldsymbol{E} = \begin{bmatrix} E_{\xi\xi} & E_{\xi\eta} & E_{\xi\zeta} \\ E_{\eta\xi} & E_{\eta\eta} & E_{\eta\zeta} \\ E_{\zeta\xi} & E_{\zeta\eta} & E_{\zeta\zeta} \end{bmatrix} \boldsymbol{e}_i \otimes \boldsymbol{e}_j \text{ with } i, j \in \{\xi, \eta, \zeta\}. \tag{17}$$

9

261 The EAS-method [70, 71, 72] is the first technique employed to avoid numerical locking. This method
262 involves the decomposition of the total strain tensor $\boldsymbol{E}$ into a compatible part $\boldsymbol{E}_{\mathrm{C}}$ and an enhanced part $\boldsymbol{E}_{\mathrm{e}}$

$$\boldsymbol{E} = \boldsymbol{E}_{\mathrm{C}}(\boldsymbol{u}_I) + \boldsymbol{E}_{\mathrm{e}}. \tag{18}$$

263 The compatible strain $\boldsymbol{E}_{\mathrm{C}}$ is exclusively dependent on the node displacements $\boldsymbol{u}_I$ while $\boldsymbol{E}_{\mathrm{e}}$ covers deforma-
264 tion modes incompatible with the linear shape functions. Consequently, the corresponding weak forms for
265 explicit time integration schemes read [36]

$$g_1(\boldsymbol{u}, \boldsymbol{E}_{\mathrm{e}}) = \int_{V_0} \boldsymbol{S}(\boldsymbol{E}) \cdot \delta\boldsymbol{E}_{\mathrm{C}} \, \mathrm{d}V + \int_{V_0} \rho_0 \ddot{\boldsymbol{u}} \cdot \delta\boldsymbol{u} \, \mathrm{d}V + g_{\mathrm{ext}} = 0; \tag{19}$$

$$g_2(\boldsymbol{u}, \boldsymbol{E}_{\mathrm{e}}) = \int_{V_0} \boldsymbol{S}(\boldsymbol{E}) \cdot \delta\boldsymbol{E}_{\mathrm{e}} \, \mathrm{d}V = 0; \tag{20}$$

266 where $\boldsymbol{S}$ is the second Piola-Kirchhoff stress tensor, ρ_0 is the material density, $\boldsymbol{u}$ is the displacement field
267 and g_{ext} is the external work. In the present work, the enhanced strain $\boldsymbol{E}_{\mathrm{e}}$ is introduced as

$$\boldsymbol{E}_{\mathrm{e}} = \alpha_{\mathrm{e}} \boldsymbol{B}_{\mathrm{e}} \quad \text{with} \quad \boldsymbol{B}_{\mathrm{e}} = \zeta \boldsymbol{e}_\zeta \otimes \boldsymbol{e}_\zeta, \tag{21}$$

268 where α_{e} is an enhanced degree of freedom (EAS-DOF). The EAS concept has been demonstrated to
269 facilitate the avoidance of volumetric locking phenomena and maintain optimal performance for nearly
270 incompressible materials in problems dominated by bending [72]. The approach in Equation (21) was
271 introduced by Schwarze and Reese [40] and was verified by Pagani et al. [36] for the explicit formulation.
272 A comprehensive overview of the discretization and the integration of the weak form within the utilized
273 solid-shell element can be found in Pagani et al. [36].

274 The second technique to prevent locking phenomena is the so-called ANS-method, which was first pro-
275 posed by Bathe and Dvorkin [73]. The evaluation is based on a reinterpolation of shear terms from assumed
276 shear locking-free collocation points, which are located on the elements' edges (cf. Figure 1b). The values of
277 these shear terms are then interpolated within the reference element. This approach has been demonstrated
278 to circumvent both transversal shear locking and curvature thickness locking [74, 35]. The transverse normal
279 strain $E_{\mathrm{c},\zeta\zeta}$ is modified to avoid curvature thickness locking [75, 76].

$$E_{\mathrm{c},\zeta\zeta}(\xi, \eta) = \sum_{P_{\zeta\zeta}=\mathrm{A}}^{\mathrm{D}} \frac{1}{4} \left(1 + \xi_{P_{\zeta\zeta}}\xi\right) \left(1 + \eta_{P_{\zeta\zeta}}\eta\right) E_{\mathrm{c},\zeta\zeta}(\boldsymbol{\xi}_{P_{\zeta\zeta}}). \tag{22}$$

280 The utilized collocation points $P_{\zeta\zeta} = \{A, B, C, D\}$ are located on the edges of the $(\boldsymbol{e}_\xi, \boldsymbol{e}_\eta)$-plane of the
281 element (cf. Figure 1b). The strain components $E_{\mathrm{c},\eta\zeta}$ and $E_{\mathrm{c},\xi\zeta}$ are modified to avoid transveral shear
282 locking [73, 35]

$$E_{\mathrm{c},\eta\zeta}(\xi, \zeta) = \sum_{P_{\eta\zeta}=\mathrm{E}}^{\mathrm{H}} \frac{1}{4} \left(1 + \xi_{P_{\eta\zeta}}\xi\right) \left(1 + \zeta_{P_{\eta\zeta}}\zeta\right) E_{\mathrm{c},\eta\zeta}(\boldsymbol{\xi}_{P_{\eta\zeta}}) \tag{23}$$

$$E_{\mathrm{c},\xi\zeta}(\eta, \zeta) = \sum_{P_{\xi\zeta}=\mathrm{J}}^{\mathrm{M}} \frac{1}{4} \left(1 + \eta_{P_{\xi\zeta}}\eta\right) \left(1 + \zeta_{P_{\xi\zeta}}\zeta\right) E_{\mathrm{c},\xi\zeta}(\boldsymbol{\xi}_{P_{\xi\zeta}}). \tag{24}$$

10

₂₈₃ The utilized collocation points $P_{\eta\zeta} = \{E, F, G, H\}$ and $P_{\xi\zeta} = \{J, K, L, M\}$ are located on the edges of the

₂₈₄ $(\boldsymbol{e}_\xi, \boldsymbol{e}_\zeta)$-plane and $(\boldsymbol{e}_\eta, \boldsymbol{e}_\zeta)$-plane of the element, respectively (cf. Figure 1b).

₂₈₅ All integration points of the solid-shell element are situated in the normal trough the element center

₂₈₆ $\boldsymbol{\xi}^\star = \zeta^\star \boldsymbol{e}_\zeta$ [77]. Therefore, the compatible strain $\boldsymbol{E}_{\mathrm{C}}$ can be split into a part, which is related to the strains

₂₈₇ at the integration points $\boldsymbol{E}_{\mathrm{C}}^\star = \boldsymbol{E}_{\mathrm{C}}(\boldsymbol{\xi}^\star)$ and a part called hourglass strain $\boldsymbol{E}_{\mathrm{C}}^{\mathrm{hg}}$ [40]

$$\boldsymbol{E}_{\mathrm{C}} = \boldsymbol{E}_{\mathrm{C}}^\star + \boldsymbol{E}_{\mathrm{C}}^{\mathrm{hg}}. \tag{25}$$

₂₈₈ The compatible strain $\boldsymbol{E}_{\mathrm{C}}^\star$ in Equation (25) is used to evaluate the constitutive material law at the integration

₂₈₉ points. The hourglass strain $\boldsymbol{E}_{\mathrm{C}}^{\mathrm{hg}}$ is employed to ensure the full rank of the element formulation and is

₂₉₀ therefore relevant for the numerical stability of the element. To calculate the two parts of the compatible

₂₉₁ strain $\boldsymbol{E}_{\mathrm{C}}$, it is expanded in a Taylor series around the element center $\boldsymbol{\xi}^0 = \boldsymbol{0}$ [40]

$$\boldsymbol{E}_{\mathrm{C}} = \underbrace{\boldsymbol{E}_{\mathrm{C}}^0 + \zeta\boldsymbol{E}_{\mathrm{C}}^\zeta + \zeta^2\boldsymbol{E}_{\mathrm{C}}^{\zeta\zeta}}_{\boldsymbol{E}_{\mathrm{C}}^\star} + \underbrace{\xi\boldsymbol{E}_{\mathrm{C}}^\xi + \eta\boldsymbol{E}_{\mathrm{C}}^\eta + \xi\eta\boldsymbol{E}_{\mathrm{C}}^{\xi\eta} + \xi\zeta\boldsymbol{E}_{\mathrm{C}}^{\xi\zeta} + \eta\zeta\boldsymbol{E}_{\mathrm{C}}^{\eta\zeta}}_{\boldsymbol{E}_{\mathrm{C}}^{\mathrm{hg}}} \quad \text{with} \quad \boldsymbol{E}_{\mathrm{C}}^{\xi_i} = \left(\frac{\partial \boldsymbol{E}_{\mathrm{C}}}{\partial \xi_i}\right)_{\boldsymbol{\xi}=\boldsymbol{\xi}^0}. \tag{26}$$

₂₉₂ The tensor-valued derivatives $\boldsymbol{E}_{\mathrm{C}}^{\xi_i}$ are explicitly given, e.g., by Schwarze and Reese [40]. Note, that the strain

₂₉₃ $\boldsymbol{E}_{\mathrm{C}}^\star$ in Equation (26) is quadratic in ζ which was found to be more accurate than a linear approximation

₂₉₄ [40].

₂₉₅ Analogous, a Taylor expansion with respect to the element center $\boldsymbol{\xi}^0 = \boldsymbol{0}$ is applied on the second

₂₉₆ Piola-Kirchhoff stress $\boldsymbol{S}$ which can be expressed as [47, 40]

$$\boldsymbol{S} = \underbrace{\boldsymbol{S}(\boldsymbol{E}^\star)}_{\boldsymbol{S}^\star} + \underbrace{\overbrace{\left(\frac{\partial \boldsymbol{S}(\boldsymbol{E})}{\partial \boldsymbol{E}}\right)_{\boldsymbol{\xi}=\boldsymbol{\xi}^0}}^{\mathbb{C}^\star}\left[\xi\boldsymbol{E}_{\mathrm{C}}^\xi + \eta\boldsymbol{E}_{\mathrm{C}}^\eta + \xi\zeta\boldsymbol{E}_{\mathrm{C}}^{\xi\zeta} + \eta\zeta\boldsymbol{E}_{\mathrm{C}}^{\eta\zeta}\right]}_{\boldsymbol{S}^{\mathrm{hg}}}. \tag{27}$$

₂₉₇ The term $\boldsymbol{S}^\star$ represents the stresses, which are evaluated at the integration points $\boldsymbol{\xi}^\star$. The term $\boldsymbol{S}^{\mathrm{hg}}$

₂₉₈ represents the hourglass stresses. Note, that the stiffness tangent $\mathbb{C}^\star$ at the element center $\boldsymbol{\xi}^0$ can be

₂₉₉ material- and deformation-dependent. To enable and analytical integration of the hourglass stresses, the

₃₀₀ stiffness tangent $\mathbb{C}^\star$ is approximated by a constant stiffness tensor $\mathbb{C}^{\mathrm{hg}}$ [60].

₃₀₁ For a more thorough exposition of the fundamental formulation of the solid-shell element and its imple-

₃₀₂ mentation, the reader is directed to the original publications [39, 40, 36].

₃₀₃ *3.2.2. Membrane-bending decomposition*

₃₀₄ In order to accurately simulate the forming process of CoFRTPs, the presented solid-shell element requires

₃₀₅ a membrane-bending decomposition similar to the one used in the 2D approach. The methodology to achieve

₃₀₆ this decomposition is based on the work of Schäfer et al. [60, 61] and is briefly outlined in the following.

₃₀₇ The total strain $\boldsymbol{E}$ is decomposed into a part that is constant over the thickness of the solid-shell element,

₃₀₈ the membrane strain $\boldsymbol{E}^{\mathrm{M}}$, and a part that varies over the thickness of the solid-shell element, the bending

11

309 strain $\boldsymbol{E}^{\mathrm{B}}$,

$$\boldsymbol{E} = \boldsymbol{E}_{\mathrm{e}} + \boldsymbol{E}_{\mathrm{C}} = \overbrace{\underbrace{\boldsymbol{E}_{\mathrm{e}} + \boldsymbol{E}_{\mathrm{C}}^{0}}_{\boldsymbol{E}^{\mathrm{M}}} + \underbrace{\zeta \boldsymbol{E}_{\mathrm{C}}^{\zeta} + \zeta^{2} \boldsymbol{E}_{\mathrm{C}}^{\zeta\zeta}}_{\boldsymbol{E}^{\mathrm{B}}}}^{\boldsymbol{E}^{\star}} + \boldsymbol{E}_{\mathrm{C}}^{\mathrm{hg}}. \tag{28}$$

310 To decompose membrane and bending deformation modes, the stresses relevant for the integration scheme
311 of the solid-shell element $\boldsymbol{S}^{\star}$ are decomposed into a part that is constant over the thickness of the solid-shell
312 element, the membrane stress $\boldsymbol{S}^{\mathrm{M}}$, and a part that varies over the thickness of the solid-shell element, the
313 bending stress $\boldsymbol{S}^{\mathrm{B}}$. Consequently, the total stress $\boldsymbol{S}$ can be expressed as [60, 61, 78]

$$\boldsymbol{S} = \underbrace{\boldsymbol{S}^{\mathrm{M}}\left(\boldsymbol{E}^{\mathrm{M}}\right) + \boldsymbol{S}^{\mathrm{B}}\left(\boldsymbol{E}^{\mathrm{B}}\right)}_{\boldsymbol{S}^{\star}} + \boldsymbol{S}^{\mathrm{hg}}\left(\boldsymbol{E}^{\mathrm{hg}}\right) = \mathbb{C}^{\mathrm{M}}\left[\boldsymbol{E}^{\mathrm{M}}\right] + \mathbb{C}^{\mathrm{B}}\left[\boldsymbol{E}^{\mathrm{B}}\right] + \mathbb{C}^{\mathrm{hg}}\left[\boldsymbol{E}_{\mathrm{C}}^{\mathrm{hg}}\right]. \tag{29}$$

314 As demonstrated by Schäfer et al. [60], the decomposition method outlined in Equation (29) enables the
315 isolation of the material response into membrane and bending deformation modes. For the hourglass stabi-
316 lization, the hourglass stiffness

$$\left(\frac{\partial \boldsymbol{S}}{\partial \boldsymbol{E}}\right)_{\boldsymbol{\xi} = \boldsymbol{\xi}^{0}} = \mathbb{C}^{\mathrm{hg}} = \mathbb{C}^{\mathrm{M}} \tag{30}$$

317 proved to be a suitable approximation for highly anisotropic engineering textiles [60].

318 *3.2.3. Enabling rate-dependent material behavior*

319 In order to implement the Voigt-Kelvin approach, cf. Section 2.1.1, in the solid-shell element and
320 enable rate-dependent material modeling, different enhancements are necessary. First, the viscous stresses
321 in Equation (3) are a function of $\boldsymbol{D}$. The deformation rate tensor $\boldsymbol{D}$ can be calculated from the strain rate
322 tensor $\dot{\boldsymbol{E}}$ and the deformation gradient $\boldsymbol{F}$ using Equation (6). However, the deformation gradient $\boldsymbol{F}$, is not
323 directly available in the solid-shell element due to the modifications of the Green-Lagrange strain $\boldsymbol{E}$ based on
324 the EAS- and ANS-method (cf. Section 3.2.1). Consequently, the Green-Lagrange strain tensor $\boldsymbol{E}$, derived
325 from Equation (28), does not generally describe the same deformation state as the strain tensor that solely
326 results from the tri-linear shape functions (Equation (16)) and the nodes' displacements $\boldsymbol{u}_{I}$. Therefore, an
327 appropriate approximation $\boldsymbol{F}_{\mathrm{tec}}$ for $\boldsymbol{F}$ in dependence on a modified strain tensor $\boldsymbol{E}_{\mathrm{mod}}$ is required.

328 Hauptmann et al. [43] and Mitsch et al. [62] proposed a routine for a suitable approximation $\boldsymbol{F}_{\mathrm{tec}}$ in de-
329 pendence on modified strain measurements $\boldsymbol{E}_{\mathrm{mod}}$. To this end, the polar decomposition for the deformation
330 gradient $\boldsymbol{F}_{\mathrm{tec}}$ is employed [66]

$$\boldsymbol{F}_{\mathrm{tec}} = \boldsymbol{R}\boldsymbol{U}_{\mathrm{tec}}. \tag{31}$$

331 The symmetric second-order tensor $\boldsymbol{U}_{\mathrm{tec}}$ is referred to as the stretch tensor and can be calculated from a
332 modified Green-Lagrange strain tensor $\boldsymbol{E}_{\mathrm{mod}}$ using

$$\left(\boldsymbol{U}_{\mathrm{tec}}\right)^{2} = 2\boldsymbol{E}_{\mathrm{mod}} + \boldsymbol{I} \tag{32}$$

333 where $\boldsymbol{I}$ is the second-order identity tensor. The orthogonal second-order tensor $\boldsymbol{R}$ in Equation (31) describes
334 the rigid body rotation in $\boldsymbol{F}_{\mathrm{tec}}$ and is calculated using the polar decomposition of the deformation gradient
335 $\boldsymbol{F}$ which corresponds to the original node displacements $\boldsymbol{u}_{I}$. Subsequently, the approximated deformation
336 gradient $\boldsymbol{F}_{\mathrm{tec}}$ can be calculated (Equation (31)). It is then used to calculate the viscous Cauchy stress tensor

12

$\boldsymbol{\sigma}^{\text{visc}}$ (Equation (3)) and the corresponding second Piola-Kirchhoff stress tensor $\boldsymbol{S}^{\text{visc}}$ (Equation (7)). Finally, the rate-dependent material behavior of the solid-shell element can be applied as constitutive equations for the membrane and the bending behavior. The corresponding stress reads

$$S = \underbrace{S_{\text{M}}\left(E_{\text{M}}, \dot{E}_{\text{M}}\right) + S_{\text{B}}\left(E_{\text{B}}, \dot{E}_{\text{B}}\right)}_{S^{\star}} + S^{\text{hg}}. \tag{33}$$

As demonstrated by Mitsch et al. [62], this approach enables the description of the rate-dependent material behavior of the solid-shell element, while ensuring the preservation of membrane-bending decomposition.

With the introduction of rate-dependency, the Taylor expansion of the total stress $\boldsymbol{S}(\boldsymbol{E}, \dot{\boldsymbol{E}})$ around the element center $\boldsymbol{\xi}^0$ (cf. Equation (27)) now includes derivatives with respect to both the strain $\boldsymbol{E}$ and the strain rate $\dot{\boldsymbol{E}}$. Therefore, the hourglass stress $\boldsymbol{S}^{\text{hg}}$ is no longer solely dependent on the strain $\boldsymbol{E}$, but also on the strain rate $\dot{\boldsymbol{E}}$. In earlier work on anisotropic elasticity [60, 61], the hourglass stabilization was based on the material tangent evaluated in the mid-plane of the element, which proved effective for the purely elastic case (cf. Equation (30)). The concept to use the material's resistance against deformation in the mid-plane of the element $\boldsymbol{\xi}^0$ to calculate the hourglass stress is now extended to the rate-dependent case. Specifically, the material tangent with respect to the strain rate $\dot{\boldsymbol{E}}$ is used to represent the viscous contribution in the hourglass stabilization. The contribution of rate-dependent hourglass stress $\boldsymbol{S}^{\text{hg}}_{\text{visc}}$ to the total stress can be considered by decomposing the hourglass stress $\boldsymbol{S}^{\text{hg}}$ into an elastic part $\boldsymbol{S}^{\text{hg}}_{\text{elast}}$ and a viscous part $\boldsymbol{S}^{\text{hg}}_{\text{visc}}$ using the Voigt-Kelvin approach (Equation (1)),

$$S^{\text{hg}} = \overbrace{\underbrace{\left(\frac{\partial S_{\text{elast}}(E)}{\partial E}\right)_{\boldsymbol{\xi}=\boldsymbol{\xi}^0}}_{\mathbb{C}^{\star}}\left[E_{\text{C}}^{\text{hg}}\right]}^{S^{\text{hg}}_{\text{elast}}} + \overbrace{\underbrace{\left(\frac{\partial S_{\text{visc}}(\dot{E})}{\partial \dot{E}}\right)_{\boldsymbol{\xi}=\boldsymbol{\xi}^0}}_{\mathbb{V}^{\star}}\left[\dot{E}_{\text{C}}^{\text{hg}}\right]}^{S^{\text{hg}}_{\text{visc}}}. \tag{34}$$

The tensor $\mathbb{V}^{\star}$ in Equation (34) represents the hourglass viscosity tensor, which serves as the viscous counterpart to the hourglass stiffness tensor $\mathbb{C}^{\star}$. The derivation of the hourglass viscosity tensor $\mathbb{V}^{\star}$ is described in detail in Appendix A. The viscous hourglass stresses $\boldsymbol{S}^{\text{hg}}_{\text{visc}}$ are calculated using Equation (A.8)

$$\begin{aligned} S_{\text{visc}}^{\text{hg}} = \mathbb{V}^{\star}\left[\dot{E}_{\text{C}}^{\text{hg}}\right] &= \mathbb{V}^{\star}\left[\xi \dot{E}_{\text{C}}^{\xi} + \eta \dot{E}_{\text{C}}^{\eta} + \xi\eta \dot{E}_{\text{C}}^{\xi\eta} + \xi\zeta \dot{E}_{\text{C}}^{\xi\zeta} + \eta\zeta \dot{E}_{\text{C}}^{\eta\zeta}\right] \\ &= J\eta^{\text{M}}\boldsymbol{C}^{-1}\left(\xi \dot{E}_{\text{C}}^{\xi} + \eta \dot{E}_{\text{C}}^{\eta} + \xi\eta \dot{E}_{\text{C}}^{\xi\eta} + \xi\zeta \dot{E}_{\text{C}}^{\xi\zeta} + \eta\zeta \dot{E}_{\text{C}}^{\eta\zeta}\right)\boldsymbol{C}^{-1}, \end{aligned} \tag{35}$$

where η^{M} is the material's viscosity in the mid-plane $\boldsymbol{\xi} = \boldsymbol{0}$ of the solid-shell element. The tensor $\boldsymbol{C} = \boldsymbol{F}^{\text{T}}\boldsymbol{F}$ is the right Cauchy-Green tensor which was obtained using $\boldsymbol{F}_{\text{tec}}$ from Equation (31) and J is the determinant of $\boldsymbol{F}_{\text{tec}}$.

3.2.4. Parameters of the 3D material model

As this work investigates the correspondence of material parameters using different element formulations, a brief summary of the material parameters utilized in the solid-shell element is provided in the following.

Two elastic stiffness tensors $\mathbb{C}^{\text{3D,M}}$ and $\mathbb{C}^{\text{3D,B}}$ are defined for the elastic membrane and bending behavior.

13

³⁶³ The elastic law for the membrane behavior in Voigt-notation reads (cf. Equation (2))

$$
\underbrace{\begin{bmatrix} C_{11}^{3D,M} & 0 & 0 & 0 & 0 & 0 \\ 0 & C_{22}^{3D,M} & 0 & 0 & 0 & 0 \\ 0 & 0 & C_{33}^{3D,M} & 0 & 0 & 0 \\ 0 & 0 & 0 & C_{44}^{3D,M} & 0 & 0 \\ 0 & 0 & 0 & 0 & C_{55}^{3D,M} & 0 \\ 0 & 0 & 0 & 0 & 0 & C_{66}^{3D,M} \end{bmatrix}}_{\hat{=}\,\mathbb{C}^{3D,M}} \underbrace{\begin{bmatrix} E_{11}^{3D,M} \\ E_{22}^{3D,M} \\ E_{33}^{3D,M} \\ 2E_{12}^{3D,M} \\ 2E_{23}^{3D,M} \\ 2E_{13}^{3D,M} \end{bmatrix}}_{\hat{=}\,\boldsymbol{E}^{3D,M}} = \underbrace{\begin{bmatrix} S_{11}^{3D,M} \\ S_{22}^{3D,M} \\ S_{33}^{3D,M} \\ S_{12}^{3D,M} \\ S_{23}^{3D,M} \\ S_{13}^{3D,M} \end{bmatrix}}_{\hat{=}\,\boldsymbol{S}_{\mathrm{elast}}^{3D,M}}.
\tag{36}
$$

³⁶⁴ The parameters $C_{11}^{3D,M}$, $C_{22}^{3D,M}$ and $C_{44}^{3D,M}$ describe the in-plane stiffnesses of the solid-shell element analogous
³⁶⁵ to the membrane stiffnesses of the 2D approach, cf. Equation (13). The parameters $C_{33}^{3D,M}$, $C_{55}^{3D,M}$ and $C_{66}^{3D,M}$
³⁶⁶ describe the out-of-plane stiffnesses of the elements mid-plane ($\zeta^\star = 0$). In this context, $C_{33}^{3D,M}$ is the stiffness
³⁶⁷ in the $\boldsymbol{e}_\zeta$-direction, respectively the compaction stiffness of the solid-shell element C_{C}, cf. Equation (8).
³⁶⁸ The parameters $C_{55}^{3D,M}$ and $C_{66}^{3D,M}$ are the shear stiffnesses in the ($\boldsymbol{e}_\zeta$-$\boldsymbol{e}_\xi$)- and ($\boldsymbol{e}_\zeta$-$\boldsymbol{e}_\eta$)-plane, corresponding
³⁶⁹ to the transversal shear stiffnesses of the solid-shell element.

³⁷⁰ The elastic law for the bending behavior in Voigt-notation reads (cf. Equation (2))

$$
\underbrace{\begin{bmatrix} C_{11}^{3D,B} & 0 & 0 & 0 & 0 & 0 \\ 0 & C_{22}^{3D,B} & 0 & 0 & 0 & 0 \\ 0 & 0 & C_{33}^{3D,B} & 0 & 0 & 0 \\ 0 & 0 & 0 & C_{44}^{3D,B} & 0 & 0 \\ 0 & 0 & 0 & 0 & C_{55}^{3D,B} & 0 \\ 0 & 0 & 0 & 0 & 0 & C_{66}^{3D,B} \end{bmatrix}}_{\hat{=}\,\mathbb{C}^{3D,B}} \underbrace{\begin{bmatrix} E_{11}^{3D,B} \\ E_{22}^{3D,B} \\ E_{33}^{3D,B} \\ 2E_{12}^{3D,B} \\ 2E_{23}^{3D,B} \\ 2E_{13}^{3D,B} \end{bmatrix}}_{\hat{=}\,\boldsymbol{E}^{3D,B}} = \underbrace{\begin{bmatrix} S_{11}^{3D,B} \\ S_{22}^{3D,B} \\ S_{33}^{3D,B} \\ S_{12}^{3D,B} \\ S_{23}^{3D,B} \\ S_{13}^{3D,B} \end{bmatrix}}_{\hat{=}\,\boldsymbol{S}_{\mathrm{elast}}^{3D,B}}.
\tag{37}
$$

³⁷¹ The parameters $C_{11}^{3D,B}$, $C_{22}^{3D,B}$ and $C_{44}^{3D,B}$ describe the elastic bending behavior in the ($\boldsymbol{e}_\xi$-$\boldsymbol{e}_\eta$)-plane, anal-
³⁷² ogous to the bending stiffnesses of the 2D approach, cf. Equation (15). The parameter $C_{33}^{3D,B}$ describes
³⁷³ the correlation between the compaction strains, which vary over the thickness of the solid-shell element,
³⁷⁴ $E_{33}^{3D,B}$, an the corresponding bending stresses $S_{33}^{3D,B}$. Since varying compaction strains E_{33}^{B} lack physical
³⁷⁵ meaning, the parameter $C_{33}^{3D,B}$ is set close to zero to inhibit the introduction of stresses or forces due to
³⁷⁶ this deformation mode and prevent numerical instabilities. The parameters $C_{55}^{3D,B}$ and $C_{66}^{3D,B}$ describe the
³⁷⁷ stiffnesses corresponding to varying transversal shear strains $E_{55}^{3D,B}$ and $E_{66}^{3D,B}$.

³⁷⁸ Poisson's ratios are not explicitly included in the elastic stiffness tensors $\mathbb{C}^{3D,M}$ and $\mathbb{C}^{3D,B}$, consistent
³⁷⁹ with the earlier 2D approaches [16]. Their effects are implicitly captured through the isotropic assumption
³⁸⁰ of the viscous material model. The viscous behavior for both the membrane and bending behavior follows
³⁸¹ an isotropic Newtonian model (Equation (3)) extended by a nonlinear Cross viscosity law (Equation (4))
³⁸² analogous to the 2D approach, cf. (Section 3.1.2).

³⁸³ *3.2.5. Remarks on the avoidance of locking phenomena for forming simulation of CoFRTPs*

³⁸⁴ While the fundamental element formulation of the solid-shell element addresses the avoidance of trans-
³⁸⁵ verse shear locking and volumetric locking phenomena, it does not inherently prevent tensile locking phe-

14

nomena, which can occur in the case of highly anisotropic materials, such as CoFRTPs. In order to avoid tensile locking phenomena, the in-plane element edges are initially aligned in fiber direction $\boldsymbol{e}_1$ and transverse direction $\boldsymbol{e}_2$ of the blank, as recommended by ten Thije and Akkerman [79]. As we found this technique to be sufficient to prevent tensile locking, no further modifications to the element formulation were carried out. Note, that Hamila and Boisse [80, 81] presented alternative approaches to circumventing tensile locking, involving modifications to the hourglass stabilization method. These approaches enable the utilization of unaligned meshes while preventing tensile locking phenomena.

The introduction of isotropic viscous contributions to the materials response induces Poisson effects even if the elastic part of the material model is free of Poisson effects. This can lead to volumetric locking phenomena, which are typically associated with nearly incompressible materials [72, 40]. While the introduction of the EAS-DOF α_e in Equation (21) effectively avoids volumetric locking in the thickness direction, no inherent prevention of volumetric locking phenomena in the in-plane directions is provided. However, the influence of volumetric locking phenomena in the in-plane directions is expected to be negligible due to the elevated material stiffness in fiber direction where the elastic forces are considerably higher than the viscous forces, effectively preventing Poisson effects in the ($\boldsymbol{e}_\xi$-$\boldsymbol{e}_\eta$)-plane and therefore preventing volumetric locking phenomena.

4. Transfer of material properties using coupon tests

4.1. Numerical setups for the coupon tests

In order to benefit from the reduced computational demands of the 2D approach for parameterization, an investigation is conducted into the transfer of in-plane and bending material properties from the element formulation employing the 2D approach outlined in Section 3.1 to the solid-shell element in Section 3.2. The workflow of transferring material parameters from the 2D approach to the 3D solid-shell approach is schematically summarized in Figure 2. To prove the validity of the proposed workflow, a series of coupon tests are conducted using the finite element software Abaqus/Explicit. Three different loading conditions are considered: pure tension, simple shear and cantilever bending. The pure tension test and the simple shear test are employed to identify the in-plane material properties, whereas the cantilever bending test is utilized to assess the bending properties. The out-of-plane compaction behavior is parametrized based on the results of the compaction tests from Xiong et al. [53], cf. Section 2.2.
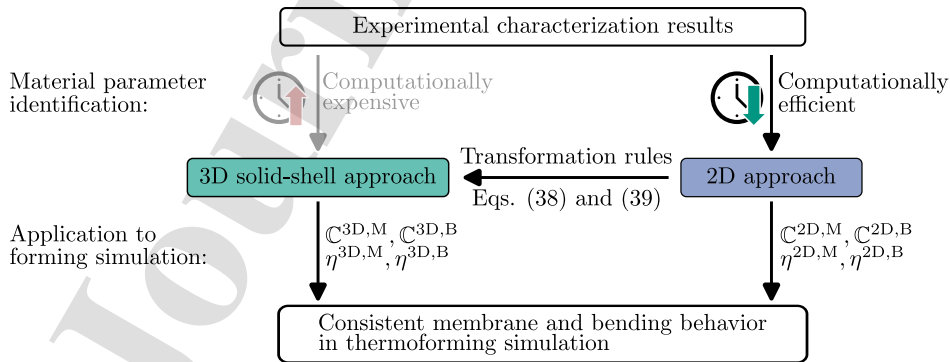

Figure 2: Schematic of material parameter transfer from the 2D approach to the 3D solid-shell approach

414 *4.2. Transformation rule for the material properties from 2D to 3D*

415 The material properties describing the membrane behavior of the solid-shell element (Section 3.2.4) are
416 connected to the material properties of the 2D approach (Section 3.1.2) using the following calculation rules

$$
\begin{aligned}
C_{11}^{\text{3D,M}} &= E_{\text{F}}^{\text{2D,M}} + E_{\text{M}}^{\text{2D,M}}, & C_{22}^{\text{3D,M}} &= E_{\text{M}}^{\text{2D,M}}, & C_{33}^{\text{3D,M}} &= C_{\text{C}}\left(E_{33}^{\text{M}}\right), \\
C_{44}^{\text{3D,M}} &= \frac{1}{2}E_{\text{M}}^{\text{2D,M}}, & C_{55}^{\text{3D,M}} &= C_{66}^{\text{3D,M}} = 10 \text{ MPa}, & \eta_0^{\text{3D,M}} &= \eta_0^{\text{2D,M}}, \\
\eta_\infty^{\text{3D,M}} &= \eta_\infty^{\text{2D,M}}, & m^{\text{3D,M}} &= m^{\text{2D,M}}, & n^{\text{3D,M}} &= n^{\text{2D,M}}.
\end{aligned}
\tag{38}
$$

417 The transverse shear stiffnesses $C_{55}^{\text{3D,M}}$ and $C_{66}^{\text{3D,M}}$ are set to 10 MPa, as these parameters have negligible
418 influence on the simulation outcome, but contribute to overall numerical stability [63]. The compaction
419 stiffness $C_{\text{C}}\left(E_{33}^{\text{M}}\right)$ is calculated at simulation runtime using the compaction model from Section 2.2.

420 The bending behavior of the solid-shell element is described using the same material parameters as for
421 the 2D approach

$$
\begin{aligned}
C_{11}^{\text{3D,B}} &= C_{11}^{\text{2D,B}}, & C_{22}^{\text{3D,B}} &= C_{22}^{\text{2D,B}}, & C_{33}^{\text{3D,B}} &= 0.01 \text{ MPa}, \\
C_{44}^{\text{3D,B}} &= C_{12}^{\text{2D,B}}, & C_{55}^{\text{3D,B}} &= C_{66}^{\text{3D,B}} = 10 \text{ MPa}, & \eta_0^{\text{3D,B}} &= \eta_0^{\text{2D,B}}, \\
\eta_\infty^{\text{3D,B}} &= \eta_\infty^{\text{2D,B}}, & m^{\text{3D,B}} &= m^{\text{2D,B}}, & n^{\text{3D,B}} &= n^{\text{2D,B}}.
\end{aligned}
\tag{39}
$$

422 As the shear stiffnesses $C_{55}^{\text{3D,B}}$, and $C_{66}^{\text{3D,B}}$ have been demonstrated to exert minimal influence on the forming
423 simulation results [63], they are each assigned a constant value of 10 MPa.

424 *4.3. Numerical verification of transferability of material parameters from 2D to 3D*

425 In order to verify that the proposed transformation rules (Equation (38) and Equation (39)) for the
426 material parameters from the 2D approach to the 3D solid-shell approach are valid, a series of numerical
427 coupon tests are conducted. The numerical coupon tests are performed using the 2D approach from Sec-
428 tion 3.1 and the 3D solid-shell element formulation from Section 3.2 with generic material parameters. The
429 generic material parameters are summarized in Appendix B and satisfy the conditions in Equation (38) and
430 Equation (39).

431 The specimen for the tensile tests are $l_{\text{T}} = 60$ mm in length, $b_{\text{T}} = 10$ mm in width, and have a thickness
432 of $t_{\text{T}} = 0.3$ mm. The specimen are fixed at the origin of the coordinate system, and the tension is applied
433 displacement-controlled. The maximum displacement is attained at $u_{\text{T}} = 10$ mm. Different deformation
434 rates $\dot{u}_{\text{T}}$ are achieved by applying the same maximum tip displacement u_{T} over different periods of time
435 T_{T}. The results are compared using the reaction forces R_1 at the tip of the tensile rods.

436 The specimen for the simple shear test is $l_{\text{Sh}} = 5$ mm in length, $b_{\text{Sh}} = 5$ mm in width, and has a thickness
437 of $t_{\text{Sh}} = 0.3$ mm. The specimen is fixed at the bottom, and the shearing is applied displacement-controlled.
438 The maximum displacement is attained at $u_{\text{Sh}} = 1$ mm. Different deformation rates $\dot{u}_{\text{Sh}}$ are achieved
439 by applying the same maximum tip displacement u_{Sh} over different periods of time T_{Sh}. The results are
440 compared using the reaction forces R_1 at the top of the specimen.

441 The specimen for the cantilever bending test is $l_{\text{B}} = 60$ mm in length, $b_{\text{B}} = 10$ mm in width, and has
442 a thickness of $t_{\text{B}} = 0.3$ mm. The beam is fixed at the origin of the coordinate system, and the bending
443 boudary condition is applied at the tip of the beam force-controlled. The maximum force is attained at

16

$R_3 = 2$ mN. The different load rates $\dot{R}_3$ are achieved by applying the same maximum load R_3 over different periods of time T_B. The results are compared using the curves of the applied reaction forces R_3 at the tip of the beam against the measured bending displacements u_3 at the tip of the beam.
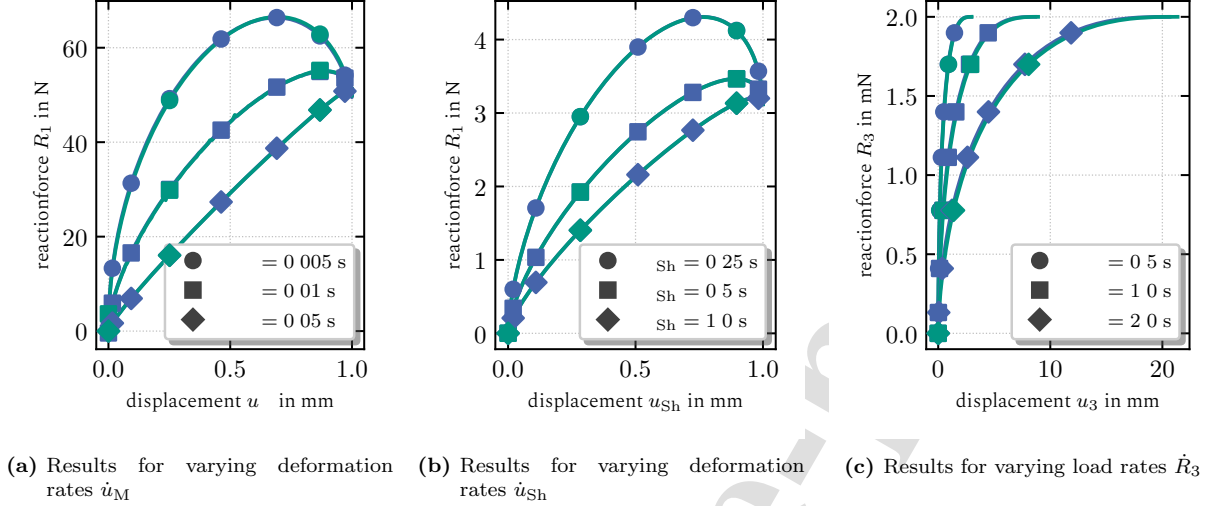

(a) Results for varying deformation rates $\dot{u}_M$
(b) Results for varying deformation rates $\dot{u}_{Sh}$
(c) Results for varying load rates $\dot{R}_3$

Figure 3: Results for the numerical coupon tests (tensile, shear, bending) under varying load rates $\dot{u}_M$, $\dot{u}_{Sh}$ and $\dot{R}_3$ using the material paramter sets from Appendix B

The results of the numerical coupon tests for tensile, shear, and bending loading conditions are presented in Figure 3a, Figure 3b, and Figure 3c, respectively. For all three loading scenarios, the responses of the 3D solid-shell element (green) show good agreement with those of the 2D approach (blue) in the rate-dependent simulations. This verifies the successful transfer of material parameters from the 2D model to the 3D solid-shell element using the transformation rules given in Equation (38) and Equation (39). As a result, the material characterization process for 3D solid-shell elements is significantly simplified, as it facilitates the utilisation of computationally efficient 2D formulations for parameter identification of the 3D approach. Note that the 2D approach utilises infinitesimal strain theory for the bending behavior (cf. Equation (15)). Consequently, for large finite bending strains $\boldsymbol{E}^{3D,B}$, the results of the bending tests may deviate from the results of the solid-shell element formulation, which employs finite strain theory.

4.4. Parameterization of the compaction behavior

In order to parameterize the compaction behavior of the solid-shell element, compaction data from literature [53] is utilised. The test setup for the compaction test is illustrated in Figure 4a. The specimen for the compaction test is $l_C = 60$ mm in length, $b_C = 60$ mm in width, and has an initial thickness of $t_C = 2.05$ mm and is situated between two rigid plates. The plate on the bottom is fixed, while the plate on the top is displaced in normal direction with $u_C = 1.2$ mm. As the experimental trial was performed with a low compaction speed of 0.2mm/s, the process can be considered quasi-static, and only the elastic compaction behavior is taken into account in the numerical compaction test. The numerical compaction test is performed using a single layer of solid-shell elements. The experimental data were digitalized using WEBPLOTDIGITIZER [82] and are displayed as green dots in Figure 4c.

17

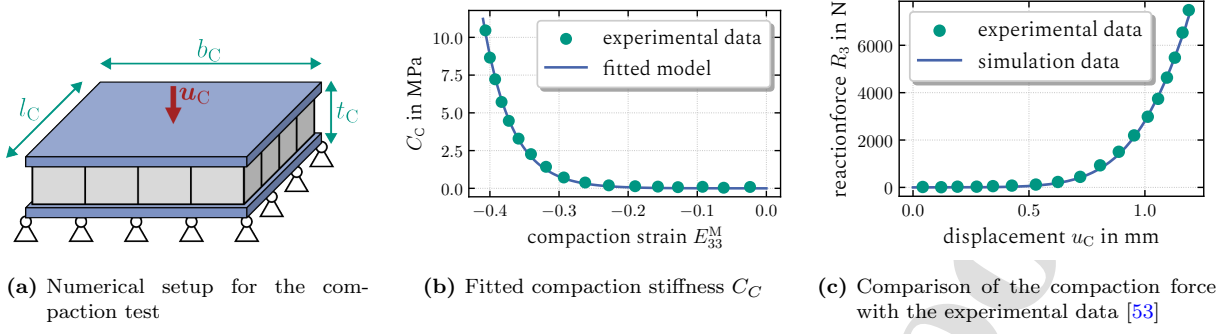**(a)** Numerical setup for the compaction test

(b) Fitted compaction stiffness C_C

(c) Comparison of the compaction force with the experimental data [53]

Figure 4: Numerical compaction test and comparison to the experimental [53].

For the nonlinear compaction behavior C_{C}, the compaction model (Equation (8)) from Section 2.2 is employed. The parameters are identified numerically using a standard nonlinear least-squares fitting procedure implemented in PYTHON. The resulting fitted parameters for C_{C} are

$$a = 5.58 \cdot 10^{-4}\ \mathrm{MPa}, \quad \text{and} \quad c = 2.416 \cdot 10^{1}. \tag{40}$$

For comparison, the corresponding compaction stiffness $C_{\mathrm{C}}^{\mathrm{exp}}$ from experimental data is calculated using

$$C_{\mathrm{C}}^{\mathrm{exp}} = \frac{S_{33}^{\mathrm{2PK}}}{E_{33}}. \tag{41}$$

and is presented in Figure 4b using green dots. The curve of the fitted compaction stiffness C_{C} (blue) is in good agreement with the analytical compaction stiffness $C_{\mathrm{C}}^{\mathrm{exp}}$ (green dots).

To validate the obtained nonlinear compaction model, the compaction stiffness C_{C} is implemented in the solid-shell element and numerical compaction tests, analogous to the setup shown in Figure 4a, are performed. The resulting curve of the compaction force R_3 versus the compaction displacement u_{C} is shown in Figure 4c as a blue line. The simulation results are in good agreement with the experimental data from Xiong et al. [53] (green dots), confirming that the proposed model accurately captures the nonlinear compaction behavior of CoFRTPs. Furthermore, the results confirm that the analytical fitting procedure is effective in determining the compaction stiffness C_{C}.

5. Application on forming simulation

In this chapter, the 3D solid-shell element formulation is employed to simulate the thermoforming process of a single layer of CoFRTP in the finite element software ABAQUS/EXPLICIT. The rate-dependent material model and the nonlinear compaction behavior are employed to represent the complex mechanical response of the material. A double-domed tool geometry is selected to investigate the forming behavior under complex deformation conditions. The results are compared against those obtained using an experimentally validated 2D approach [21] (cf. lower half of Figure 2). Finally, the thickness distribution of the formed part is evaluated to assess the solid-shell element's capability to predict local thickness changes during forming.

18

5.1. Numerical test setup for forming simulation

An illustration of the numerical test setup is shown in Figure 5. The double-dome tool geometry (green and blue) is a commonly used geometry in forming literature [e.g., 4, 83], as it includes a double curved section that requires complex deformation modes to be formed. The punch and the die geometry are modeled as rigid surfaces. The forming process is implemented in a displacement-controlled manner, applying a Dirichlet boundary condition ($u = 60$ mm) over a time period of $T = 1$ s on the punch geometry, resulting in a minimum cavity thickness of $t = 0.2$ mm at the end of the forming process.
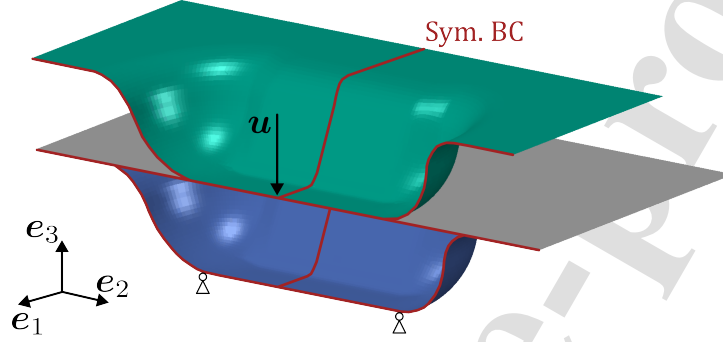
Figure 5: Numerical test setup for the forming simulation of a double-domed geometry

A single layer of CoFRTP (grey, cf. Figure 5) is formed. The original blank dimensions are 502 mm × 310 mm × 0.3 mm which are discretized (in-plane) with the element edge length of $l_e = 5$ mm and a single element in thickness direction. The element edges are initially aligned in fiber direction e_1 and transverse direction e_2 of the blank to avoid tensile locking [79, 80]. Given the twofold symmetry of the problem, only a quarter of the original problem is simulated (indicated by the red lines) resulting in a total of 1550 solid-shell elements. For the reference solution using the 2D approach, the blank is discretized with 6200 triangular shell elements. The contact between the blank and the forming tools is modeled using the general contact algorithm in ABAQUS/EXPLICIT. The tangential behavior is modeled using a Coulomb friction formulation with a friction coefficient of $\mu = 0.1$.

Two material models are investigated. The first approach utilizes a simplified viscosity model, wherein viscosity parameters remain constant throughout the forming process (Newton model). This configuration serves as a reference to isolate the influence of time-dependent viscosity effects. In order to capture the rate-dependent behavior of the material in a more realistic manner, the second setup employs a nonlinear viscosity formulation based on the Cross model, as described in Equation (4). The material parameters for both approaches are outlined in Appendix C and are based on in-house characterization trials for polypropylene reinforced with unidirectional glass fibers (PP-GF), following the methodology described by Dörr et al. [21]. Note, that the tensile stiffnesses in fiber direction are chosen well below the physically measured values for fiber stiffnesses but sufficiently high to numerically ensure the quasi-inextensibility condition of the fibers, which is a common assumption in forming simulation for composites [19, 21]. A sensitivity analysis on forming speed for both the constant and cross-type viscosity models was conducted in Appendix D.

The simulations were executed on eight cores of an AMD EPYC 74F3 processor each. The simulations employing the cross viscosity model required approximately three minutes of computation time for the

19

517 2D-approach, while the 3D solid-shell simulations required approximately nine hours of computation time.

5.2. Results and discussion

5.2.1. Constant viscosity parameters

520 The forming simulation is conducted using constant viscosities ($\eta_\infty = \eta_0$) for the membrane and bending
521 behavior to isolate the influence of time-dependent viscosity effects. The results of the forming simulation
522 for both the 3D solid-shell and the 2D approach with constant viscosity parameters are shown in Figure 6.
523 A comparison of the global deformation behavior is conducted by evaluating the displacements u_3 at three
524 representative stages of the forming process, corresponding to relative tool strokes $\Delta u = 70\%$, 80%, and
525 90% (Figure 6a). The results demonstrate that wrinkle formation occurs at equivalent locations in both
526 approaches and the maximum displacements u_3 are of comparable magnitude. The material draw-in and
527 membrane shear strain at the end of the forming process ($\Delta u = 100\%$) are shown in Figure 6b yielding
528 significantly greater material draw-in in the fiber direction e_1 than in the transverse direction e_2 in a similar
529 manner for both modeling approaches. Elevated shear strains E_{12}^{M} are observed in the double-curved regions
530 of the blank, where substantial in-plane shear deformation is required to form the geometry yielding similar
531 locations and magnitudes for both approaches. It can be concluded that the solid-shell element formulation
is capable of capturing the global forming behavior in a manner analogous to the 2D approach.
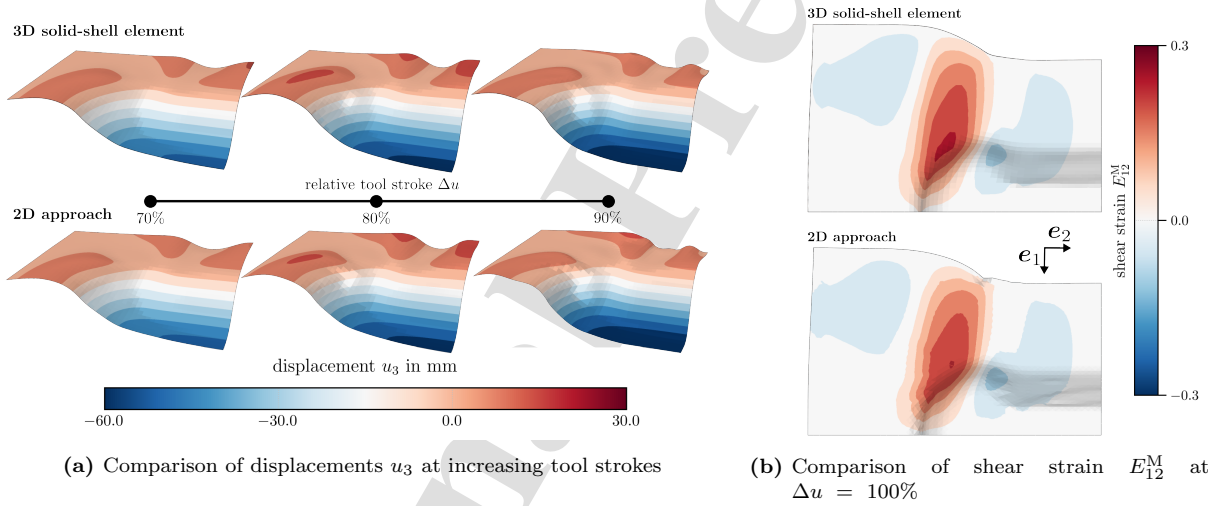

(a) Comparison of displacements u_3 at increasing tool strokes

(b) Comparison of shear strain E_{12}^{M} at $\Delta u = 100\%$

Figure 6: Comparison of the results using the 3D solid-shell versus the 2D approach using constant viscosity parameters

532

5.2.2. Cross viscosity model

534 The results of the forming simulation using the Cross viscosity model (Equation (4)) are presented in
535 Figure 7. A comparison of the global deformation behavior is conducted by evaluating the displacements
536 u_3 at three representative stages of the forming process, corresponding to relative tool strokes $\Delta u = 70\%$,
537 80%, and 90% (Figure 7a). The results demonstrate that wrinkle formation occurs at equivalent locations
538 in both approaches and the maximum displacements u_3 are of comparable magnitude. In comparison to the
539 case of constant viscosities from Section 5.2.1, the maximum displacements u_3 in positive e_3-direction are

20

considerably lower. This is because thermoplastic tapes undergo two primary deformation modes during
forming: in-plane shear and out-of-plane bending. When shear deformation is restricted due to high shear
stiffness or viscosity, bending deformations are more probable to occur, leading to the formation of wrinkles.
As the Cross viscosity model is employed, shear and bending viscosities, η^{M} and η^{B}, vary with local defor-
mation rates, $\dot{\gamma}^{\mathrm{M}}$ and $\dot{\gamma}^{\mathrm{B}}$, respectively. For the given parameter set and tool geometry, this results in a lower
effective shear viscosity η^{M} relative to the bending viscosity η^{B}, promoting shear-dominated deformation.
Consequently, less wrinkles with lower amplitudes are observed in Figure 7a than in Figure 6a. The material
draw-in and membrane shear strain at the end of the forming process ($\Delta u = 100\%$) are shown in Figure 7b
yielding significantly greater material draw-in in the fiber direction $\boldsymbol{e}_1$ than in the transverse direction $\boldsymbol{e}_2$
in a similar manner for both modeling approaches. Elevated shear strains E_{12}^{M} are observed in the double-
curved regions of the blank, where substantial in-plane shear deformation is required to form the geometry
yielding similar locations and magnitudes for both approaches. It can be concluded that the 3D solid-shell
element formulation with the employed Cross viscosity model is capable of capturing the nonlinear viscosity
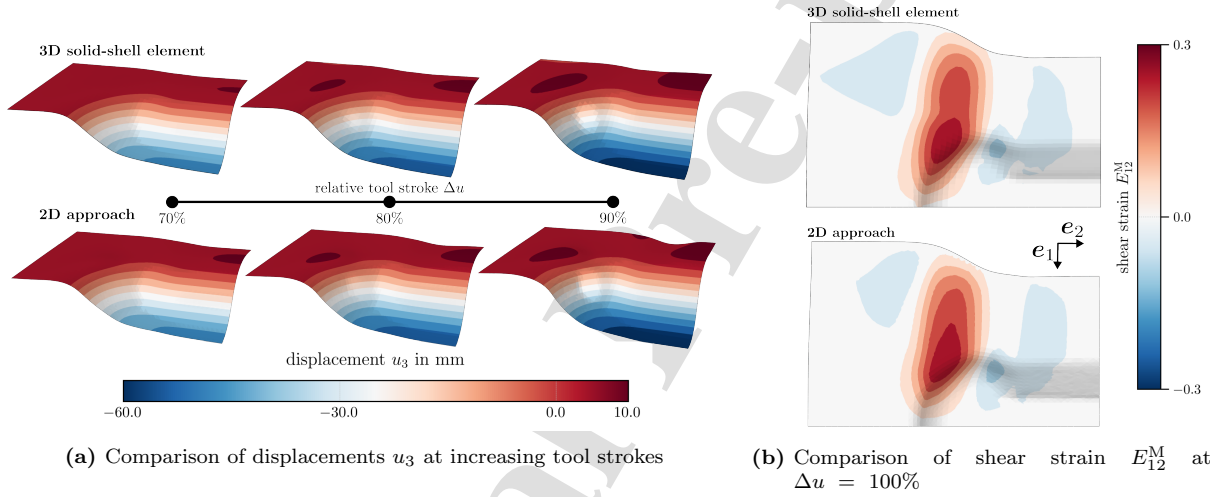behavior and the global forming behavior of the blank in a similar manner as the 2D approach.

(a) Comparison of displacements u_3 at increasing tool strokes

(b) Comparison of shear strain E_{12}^{M} at $\Delta u = 100\%$

Figure 7: Comparison of the results using the 3D solid-shell versus the 2D approach using the Cross viscosity model

5.2.3. Compaction behavior

In contrast to the 2D approach, the 3D solid-shell element formulation enables the prediction of local
thickness changes during the forming process. The final thickness distribution t at $\Delta u = 100\%$ is shown
in Figure 8. To aid visual interpretation, the right-hand side of the figure includes the double-dome tool
geometry overlaid on the blank, illustrating the regions in contact during the compaction phase of forming.
The thickness is calculated as the ratio of the solid-shell element's volume V_{e} to the average of its top and
bottom surface areas A^{Top} and A^{Bot}

$$t = \frac{2V_{\mathrm{e}}}{A^{\mathrm{Top}} + A^{\mathrm{Bot}}}. \tag{42}$$

The elements volume V_{e} and surface areas A^{Top} and A^{Bot} can obtained from the element's node coordinates
$\boldsymbol{x}_I$. The results of the elements' thicknesses indicates that the elements are compacted to a desired cavity
thickness of $t = 0.2$ mm at all locations where the blank is in contact with the forming tools. In locations

21

where the blank does not make contact with the tools, the thickness remains close to its initial value of $t_0 = 0.3$ mm. In regions where the blank bends around the tool radii, the thickness is reduced further, falling below $t = 0.2$ mm. This phenomenon can be attributed to the high curvature present in these regions, which generates increased transverse pressure as the blank is forced into the cavity.

In summary, the results qualitatively align with the anticipated outcome of compaction behavior during thermoforming and are also consistent with those shown in Xiong et al. [52, 53], Poppe et al. [56] and Schäfer [78], who also used a double-dome geometry to demonstrate through-thickness behavior. A direct quantitative comparison with experimental data is not feasible at this stage because thermoforming FRTPs with a single reinforcement direction under controlled conditions is challenging due to tearing in the unsupported transverse direction. The present results should therefore be seen as a first methodological demonstration of the solid-shell element's capability, with experimental validation identified as an essential step for future work.
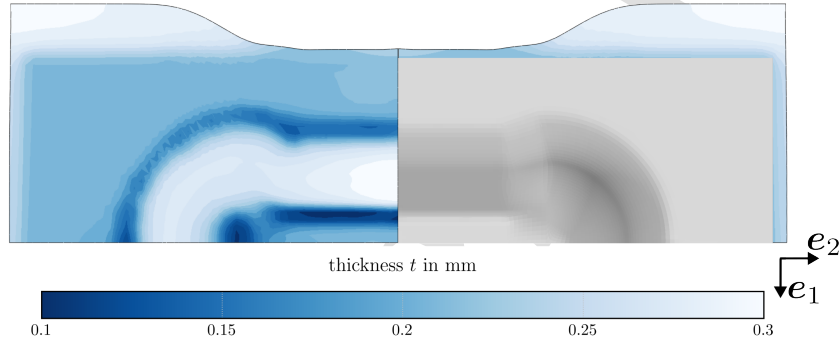

thickness t in mm

| 0.1 | 0.15 | 0.2 | 0.25 | 0.3 |

Figure 8: Resulting thickness distribution t of the forming simulation of a double-domed geometry

6. Conclusion and Outlook

In this work, a novel finite 3D element formulation based on an 8-node hexahedral solid-shell element was developed for the macroscopic simulation of the thermoforming process of CoFRTPs. This formulation enhances previous works by including rate-dependent material behavior. The solid-shell element is implemented as a VUEL user subroutine in the commercial finite element software ABAQUS/EXPLICIT. The element incorporates several numerical techniques to prevent numerical locking phenomena, such as the EAS- and the ANS-concept and utilises a tailored hourglass control scheme suitable for highly anisotropic and viscous materials, along with a membrane-bending decomposition technique.

As the characterization of the viscoelastic material model within the solid-shell element is numerically expensive, the transferability of material parameters from a 2D approach to the developed 3D solid-shell element was investigated through a series of numerical coupon tests. This facilitates the reuse of existing material datasets and significantly reduces computational expenses associated with material parameter identification. To access the performance of the developed 3D solid-shell element formulation, comparisons of the simulation results were conducted against those obtained from an experimentally validated 2D simulation

approach. Good agreement was observed between the two methods in terms of global forming behavior, material draw-in, and shear distribution, indicating that the 3D solid-shell formulation is capable of accurately capturing the key deformation mechanisms involved in the thermoforming of CoFRTPs. The evaluation of the resulting final thickness distribution yielded qualitatively expected results, thereby demonstrating the solid-shell element's ability to predict local thickness changes during the forming process which is a significant advantage compared to the 2D approach.

In summary, the proposed 3D solid-shell element formulation represents a substantial advancement in the numerical simulation of thermoforming processes for CoFRTPs. This advancement provides a more comprehensive understanding and prediction of the final part geometry, the final thickness distribution and the local fiber volume content and establishes a foundation for downstream simulation steps, including warpage and demolding simulations. Future work will include direct experimental validation of the 3D solid-shell element formulation, focusing on both the global deformation behavior and the local thickness distribution. This will involve comparing simulation results with thermoforming test data ensuring that the employed material model accurately captures the rate-dependent behavior of CoFRTPs. If discrepancies are observed, this validation will guide enhancements to the constitutive model, such as the adoption of a multi-mode viscoelastic formulation for improving accuracy. Further enhancements of the 3D solid-shell element formulation will be pursued by integrating a temperature degree of freedom. This integration will enable thermoforming simulation under varying thermal conditions, including prediction of through-thickness thermal gradients, temperature-dependent material properties, and crystallization. Beyond material modeling, the developed solid-shell formulation will be optimized in terms of computational performance. Afterwards, it will be applied to more complex geometries and multi-layered CoFRTP structures to assess its robustness and effectiveness in practical, industrial-scale thermoforming scenarios.

Author Contributions

Johannes Mitsch: Conceptualization, methodology, software, validation, formal analysis, investigation, writing–original draft preparation, visualization, analysis and interpretation of data. **Bastian Schäfer**: Conceptualization, methodology, software, writing–review and editing. **Luise Kärger**: Conceptualization, writing–review and editing, supervision, funding acquisition. All authors have read and agreed to the published version of the manuscript.

Acknowledgements

Declaration of conflicting interests

The authors declare no conflict of interest. The funders had no role in the design of the study; in the collection, analyses, or interpretation of data; in the writing of the manuscript, or in the decision to publish the results.

⁶²⁸ **Appendix A. Calculation of the hourglass stresses for viscoelastic material model**

⁶²⁹ Using the Voigt-Kelvin model (cf. Equation (1)), the viscoelastic stress is given by

$$S^{2\mathrm{PK}} = S^{2\mathrm{PK}}_{\mathrm{elas}} + S^{2\mathrm{PK}}_{\mathrm{visc}}, \tag{A.1}$$

⁶³⁰ where the elastic part is solely dependent on the elastic strain $\boldsymbol{E}$ (cf. Equation (2))

$$S^{2\mathrm{PK}}_{\mathrm{elas}} = \mathbb{C}\,[\boldsymbol{E}] \tag{A.2}$$

⁶³¹ and the viscous part is only dependent on the deformation rate tensor $\boldsymbol{D}$ (cf. Equation (1))

$$\boldsymbol{\sigma}_{\mathrm{visc}} = \eta \boldsymbol{D}. \tag{A.3}$$

⁶³² Using Equation (6), the viscous part of the second Piola-Kirchhoff stress tensor $S^{2\mathrm{PK}}_{\mathrm{visc}}$ is given by

$$S^{2\mathrm{PK}}_{\mathrm{visc}} = J\eta\,\boldsymbol{F}^{-1}\boldsymbol{D}\boldsymbol{F}^{-\mathsf{T}} = J\eta\,\boldsymbol{F}^{-1}\boldsymbol{F}^{-\mathsf{T}}\dot{\boldsymbol{E}}\boldsymbol{F}^{-1}\boldsymbol{F}^{-\mathsf{T}} = J\eta\,\boldsymbol{C}^{-1}\dot{\boldsymbol{E}}\boldsymbol{C}^{-1}, \tag{A.4}$$

⁶³³ depending on the strain rate tensor $\dot{\boldsymbol{E}}$ and utilizing the right Cauchy-Green tensor $\boldsymbol{C} = \boldsymbol{F}^{\mathsf{T}}\boldsymbol{F}$.

⁶³⁴ To calculate the contribution of the viscous stresses to the hourglass forces, the derivative of the stress
⁶³⁵ $S^{2\mathrm{PK}}$ with respect to the strain rate $\dot{\boldsymbol{E}}$ is calculated. As the elastic part of the stress $S^{2\mathrm{PK}}_{\mathrm{elast}}(\boldsymbol{E}) = \mathbb{C}\,[\boldsymbol{E}]$ is
⁶³⁶ independent of the strain rate $\dot{\boldsymbol{E}}$ the derivative of the elastic stress with respect to the strain rate $\dot{\boldsymbol{E}}$ is zero.
⁶³⁷ The derivative of the viscous part of the stress $S^{2\mathrm{PK}}_{\mathrm{visc}}(\dot{\boldsymbol{E}})$ with respect to the strain rate $\dot{\boldsymbol{E}}$ is calculated

$$\begin{aligned}
\frac{\partial S^{2\mathrm{PK}}_{\mathrm{visc},ij}}{\partial \dot{E}_{kl}} &= \frac{\partial}{\partial \dot{E}_{kl}} \left(J\eta\, C^{-1}_{im} \dot{E}_{mn} C^{-1}_{nj} \right) \\
&= \frac{J\eta}{2} \left(C^{-1}_{im} \left(\delta_{mk}\delta_{nl} + \delta_{lm}\delta_{nk} \right) C^{-1}_{nj} \right) \\
&= \frac{J\eta}{2} \left(C^{-1}_{ik} C^{-1}_{lj} + C^{-1}_{il} C^{-1}_{kj} \right) = V^{\star}_{ijkl},
\end{aligned} \tag{A.5}$$

⁶³⁸ which reads in symbolic notation

$$\frac{\partial S^{2\mathrm{PK}}_{\mathrm{visc}}(\dot{\boldsymbol{E}})}{\partial \dot{\boldsymbol{E}}} = \frac{J\eta}{2} \left(\boldsymbol{C}^{-1} \square \boldsymbol{C}^{-1} + \left(\boldsymbol{C}^{-1} \square \boldsymbol{C}^{-1} \right)^{\mathsf{T_R}} \right) = \mathbb{V}^{\star}. \tag{A.6}$$

⁶³⁹ Here, δ_{ij} denotes the Kronecker symbol. The product $\boldsymbol{A}\square\boldsymbol{B}$ is defined $(\boldsymbol{A}\square\boldsymbol{B})\,[\boldsymbol{C}] = \boldsymbol{A}\boldsymbol{C}\boldsymbol{B}$. The tensor
⁶⁴⁰ $\mathbb{V}^{\star}$ is the hourglass viscosity tensor introduced in Equation (34). Note, that if a symmetric second-order

641 tensor $\boldsymbol{A} \in Sym$ is applied on the result of Equation (A.5) simplifies to

$$
\begin{aligned}
\frac{\partial S^{\mathrm{2PK}}_{\mathrm{visc},ij}}{\partial \dot{E}_{kl}} A_{kl} &= \frac{1}{2} \frac{\partial S^{\mathrm{2PK}}_{\mathrm{visc},ij}}{\partial \dot{E}_{kl}} \left(A_{kl} + A_{kl}^{\mathsf{T}} \right) \\
&= \frac{J\eta}{4} \left(C_{ik}^{-1} C_{lj}^{-1} + C_{il}^{-1} C_{kj}^{-1} \right) \left(A_{kl} + A_{lk} \right) \\
&= \frac{J\eta}{4} \left(C_{ik}^{-1} C_{lj}^{-1} A_{kl} + C_{il}^{-1} C_{kj}^{-1} A_{kl} + C_{il}^{-1} C_{kj}^{-1} A_{kl} + C_{ik}^{-1} C_{lj}^{-1} A_{kl} \right) \\
&= J\eta C_{ik}^{-1} C_{lj}^{-1} A_{kl} \quad \forall \boldsymbol{A} \in Sym.
\end{aligned}
\tag{A.7}
$$

642 The symbolic representation of Equation (A.7) reads

$$
\frac{\partial \boldsymbol{S}^{\mathrm{2PK}}_{\mathrm{visc}}(\dot{\boldsymbol{E}})}{\partial \dot{\boldsymbol{E}}} [\boldsymbol{A}] = \mathbb{V}^{\star}[\boldsymbol{A}] = J\eta \left(\boldsymbol{C}^{-1} \square \boldsymbol{C}^{-1} \right) [\boldsymbol{A}] = J\eta \, \boldsymbol{C}^{-1} \boldsymbol{A} \boldsymbol{C}^{-1} \quad \forall \boldsymbol{A} \in Sym.
\tag{A.8}
$$

643 **Appendix B. Material parameters for the numerical coupon tests**

Table B.1: Viscoelastic membrane material parameters for the 2D approach in the the coupon tests

$E_{\mathrm{F}}^{\mathrm{2D,M}}$	$E_{\mathrm{M}}^{\mathrm{2D,M}}$	$G_{\mathrm{M}}^{\mathrm{2D,M}}$	$\eta_0^{\mathrm{2D,M}}$	$\eta_\infty^{\mathrm{2D,M}}$	$m^{\mathrm{2D,M}}$	$n^{\mathrm{2D,M}}$
MPa	MPa	MPa	MPa$\cdot$s	MPa$\cdot$s	–	–
980.0	20.0	10.0	4.0	1.0	50.9773	0.4655

Table B.2: Viscoelastic bending material parameters for the 2D approach in the the coupon tests

$C_{11}^{\mathrm{2D,B}}$	$C_{22}^{\mathrm{2D,B}}$	$C_{12}^{\mathrm{2D,B}}$	$\eta_0^{\mathrm{2D,B}}$	$\eta_\infty^{\mathrm{2D,B}}$	$m^{\mathrm{2D,B}}$	$n^{\mathrm{2D,B}}$
MPa	MPa	MPa	MPa$\cdot$s	MPa$\cdot$s	–	–
100.0	100.0	1.0	500.0	10.0	41.7412	0.6877

Table B.3: Viscoelastic membrane material parameters for the 3D approach in the the coupon tests

$C_{11}^{\mathrm{3D,M}}$	$C_{22}^{\mathrm{3D,M}}$	$C_{33}^{\mathrm{3D,M}}$	$C_{44}^{\mathrm{3D,M}}$	$C_{55}^{\mathrm{3D,M}}$	$C_{66}^{\mathrm{3D,M}}$	$\eta_0^{\mathrm{3D,M}}$	$\eta_\infty^{\mathrm{3D,M}}$	$m^{\mathrm{3D,M}}$	$n^{\mathrm{3D,M}}$
MPa	MPa	MPa	MPa	MPa	MPa	MPa$\cdot$s	MPa$\cdot$s	–	–
1000.0	20.0	20.0	10.0	10.0	10.0	4.0	1.0	50.9773	0.4655

Table B.4: Viscoelastic bending material parameters for the 3D approach in the the coupon tests

$C_{11}^{\mathrm{3D,B}}$	$C_{22}^{\mathrm{3D,B}}$	$C_{33}^{\mathrm{3D,B}}$	$C_{44}^{\mathrm{3D,B}}$	$C_{55}^{\mathrm{3D,B}}$	$C_{66}^{\mathrm{3D,B}}$	$\eta_0^{\mathrm{3D,B}}$	$\eta_\infty^{\mathrm{3D,B}}$	$m^{\mathrm{3D,B}}$	$n^{\mathrm{3D,B}}$
MPa	MPa	MPa	MPa	MPa	MPa	MPa$\cdot$s	MPa$\cdot$s	–	–
100.0	100.0	0.01	1.0	10.0	10.0	500.0	10.0	41.7412	0.6877

Appendix C. Material parameters for the forming simulation

Appendix C.1. Material parameters for the 2D approach using superimposed conventional shell elements

Table C.5: Viscoelastic model parameters for PP-GF of the membrane behavior of the conventional shell elements

Model	$E_{\mathrm{F}}^{\mathrm{2D,M}}$ MPa	$E_{\mathrm{M}}^{\mathrm{2D,M}}$ MPa	$G_{\mathrm{M}}^{\mathrm{2D,M}}$ MPa	$\eta_0^{\mathrm{2D,M}}$ MPa $\cdot$ s	$\eta_\infty^{\mathrm{2D,M}}$ MPa $\cdot$ s	$m^{\mathrm{2D,M}}$ –	$n^{\mathrm{2D,M}}$ –
Newton	1000.0	0.0147	0.00735	0.1	0.1	-	-
Cross	1000.0	0.0147	0.00735	0.4	0.0	50.9773	0.4655

Table C.6: Viscoelastic model parameters for PP-GF of the bending behavior of the conventional shell elements

Model	$C_{11}^{\mathrm{2D,B}}$ MPa	$C_{22}^{\mathrm{2D,B}}$ MPa	$C_{12}^{\mathrm{2D,B}}$ MPa	$\eta_0^{\mathrm{2D,B}}$ MPa $\cdot$ s	$\eta_\infty^{\mathrm{2D,B}}$ MPa $\cdot$ s	$m^{\mathrm{2D,B}}$ –	$n^{\mathrm{2D,B}}$ –
Newton	75.8971	0.7589	0.3794855	10.0	10.0	-	-
Cross	75.8971	0.7589	0.3794855	500.0	0.0	41.7412	0.6877

Appendix C.2. Material parameters for the 3D approach using hexahedral solid-shell elements

Table C.7: Viscoelastic model parameters for PP-GF of the membrane behavior of the solid-shell elements

Model	$C_{11}^{\mathrm{3D,M}}$ MPa	$C_{22}^{\mathrm{3D,M}}$ MPa	$C_{33}^{\mathrm{3D,M}}$ MPa	$C_{44}^{\mathrm{3D,M}}$ MPa	$C_{55}^{\mathrm{3D,M}}$ MPa	$C_{66}^{\mathrm{3D,M}}$ MPa	$\eta_0^{\mathrm{3D,M}}$ MPa $\cdot$ s	$\eta_\infty^{\mathrm{3D,M}}$ MPa $\cdot$ s	$m^{\mathrm{3D,M}}$ –	$n^{\mathrm{3D,M}}$ –
Newton	1000.0147	0.0147	C_{C}	0.00735	10.0	10.0	0.1	0.1	-	-
Cross	1000.0147	0.0147	C_{C}	0.00735	10.0	10.0	0.4	0.0	50.9773	0.4655

Table C.8: Viscoelastic model parameters for PP-GF of the bending behavior of the solid-shell elements

Model	$C_{11}^{\mathrm{3D,B}}$ MPa	$C_{22}^{\mathrm{3D,B}}$ MPa	$C_{33}^{\mathrm{3D,B}}$ MPa	$C_{44}^{\mathrm{3D,B}}$ MPa	$C_{55}^{\mathrm{3D,B}}$ MPa	$C_{66}^{\mathrm{3D,B}}$ MPa	$\eta_0^{\mathrm{3D,B}}$ MPa $\cdot$ s	$\eta_\infty^{\mathrm{3D,B}}$ MPa $\cdot$ s	$m^{\mathrm{3D,B}}$ –	$n^{\mathrm{3D,B}}$ –
Newton	75.8971	0.758971	0.01	0.3794855	10.0	10.0	10.0	10.0	-	-
Cross	75.8971	0.758971	0.01	0.3794855	10.0	10.0	500.0	0.0	41.7412	0.6877

Appendix D. Sensitivity analysis of the rate-dependent material model

To assess the sensitivity of the global deformation behavior to variations in forming velocity, simulations were performed using the 3D solid-shell element. As material parameters, the viscoelastic material behavior with constant viscosity parameters (Newton model) and Cross viscosity parameters (Cross model) were used,
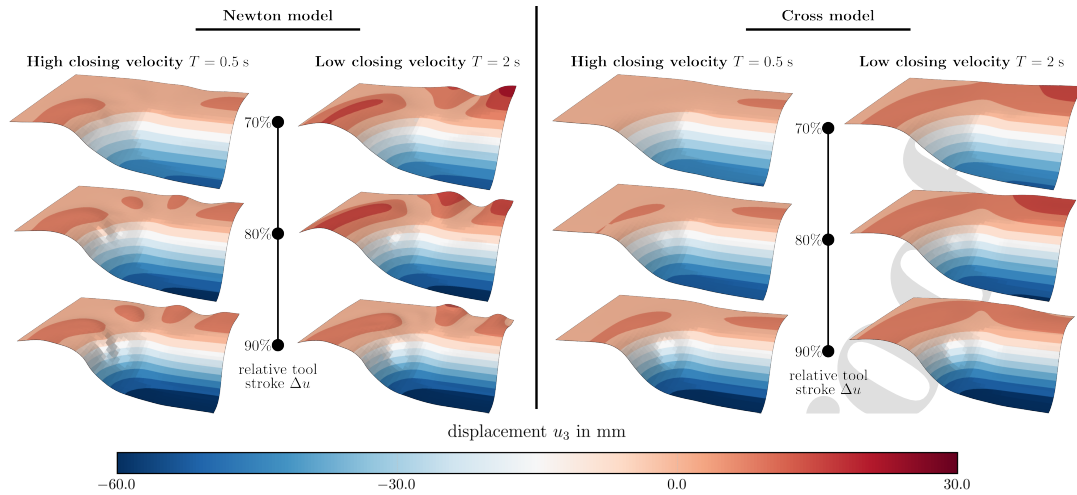
Figure D.9: Analysis of the rate-dependent material model with respect to the forming velocity

cf. Table C.7 and Table C.8. The simulation setup is the same as that described in Section 5.1. Two forming velocities were considered, corresponding to press-closing times of $T = 0.5\,\text{s}$ and $T = 2.0\,\text{s}$, respectively.

The results indicate that the Newton model (left-hand side of Figure D.9) produces significantly more wrinkles with higher amplitudes than the Cross model (right-hand side of Figure D.9), which is consistent with the findings in Section 5.2. For both models, the wrinkling amplitudes are higher at the lower forming velocity ($T = 2.0\,\text{s}$) compared to the higher forming velocity ($T = 0.5\,\text{s}$). This behavior may be attributed to higher bending viscosities relative to membrane viscosities. This effect is further superimposed by the non-linear (shear-thinning) viscosity models in case of the Cross model. Since the membrane-to-bending viscosity ratio depends on the specific viscosity parameters, these trends may vary for other material properties or geometries.

In summary, the global deformation behavior is strongly affected by forming velocity, highlighting the impact of incorporating rate-dependent material behavior in forming simulations.

References

[1] K. Vanclooster, S. van Goidsenhoven, S. V. Lomov, I. Verpoest, Optimizing the deepdrawing of multilayered woven fabric composites, International Journal of Material Forming 2 (2009) 153.

[2] H. Lessard, G. Lebrun, A. Benkaddour, X.-T. Pham, Influence of process parameters on the thermostamping of a [0/90]12 carbon/polyether ether ketone laminate, Composites Part A: Applied Science and Manufacturing 70 (2015) 59–68.

[3] U. Breuer, M. Neitzel, V. Ketzer, R. Reinicke, Deep drawing of fabric-reinforced thermoplastics: Wrinkle formation and their reduction, Polymer Composites 17 (1996) 643–647.

[4] P. Harrison, R. Gomes, N. Curado-Correia, Press forming a 0/90 cross-ply advanced thermoplastic composite using the double-dome benchmark geometry, Composites Part A: Applied Science and Manufacturing 54 (2013) 56–69.

[5] G. Zeeb, J. Mitsch, M. Wilhelm, L. Kärger, F. Henning, Influence of gripper positions on the formation of wrinkles during the thermoforming process of thermoplastic UD-tape laminates, in: Materials Research Proceedings, volume 54, Materials Research Forum LLC, 2025, pp. 544–553.

[6] T. Joppich, D. Dörr, L. van der Meulen, T. Link, B. Hangs, F. Henning, Layup and process dependent wrinkling behavior of PPS/CF UD tape-laminates during non-isothermal press forming into a complex component, in: AIP Conference Proceedings 1769, 170011, 2016, p. 170012.

27

[7] D. Brands, L. G. di Genova, E. R. Pierik, W. J. B. Grouve, S. Wijskamp, R. Akkerman, Formability Experiments for Unidirectional Thermoplastic Composites, Key Engineering Materials 926 (2022) 1358–1371.

[8] L. Kärger, S. Galkin, C. Zimmerling, D. Dörr, J. Linden, A. Oeckerath, K. Wolf, Forming optimisation embedded in a CAE chain to assess and enhance the structural performance of composite components, Composite Structures 192 (2018) 143–152.

[9] H. Chen, S. Li, J. Wang, A. Ding, A focused review on the thermo-stamping process and simulation progresses of continuous fibre reinforced thermoplastic composites, Composites Part B: Engineering 224 (2021) 109196.

[10] P. Boisse, J. Colmars, N. Hamila, N. Naouar, Q. Steer, Bending and wrinkling of composite fiber preforms and prepregs. A review and new developments in the draping simulations, Composites Part B: Engineering 141 (2018) 234–249.

[11] P. Boisse, R. Akkerman, P. Carlone, L. Kärger, S. V. Lomov, J. A. Sherwood, Advances in composite forming through 25 years of ESAFORM, International Journal of Material Forming 15 (2022) 99.

[12] H. Gunjal, G. Singh, Chapter 8 Review of optimization and simulation approaches for thermoplastic composite design, in: Green Composites Manufacturing, De Gruyter, 2024, pp. 173–198.

[13] E. Guzman Maldonado, N. Bigot, Y. Denis, N. Hamila, 13 - Thermomechanical modeling and experimental characterization of continuous fiber-reinforced thermoplastic composites at forming temperatures, in: P. Wang, N. Hamila (Eds.), Advanced Structural Textile Composites Forming, Woodhead Publishing Series in Composites Science and Engineering, Woodhead Publishing, 2025, pp. 355–388.

[14] P. P. Parlevliet, H. E. N. Bersee, A. Beukers, Residual stresses in thermoplastic composites – a study of the literature. Part III: Effects of thermal residual stresses, Composites Part A: Applied Science and Manufacturing 38 (2007) 1581–1596.

[15] X. Lu, J. Ding, X. Peng, G. Sun, X. Wang, W. Yue, H. Zhou, Z. Huang, H. Zhou, Y. W. Mai, A focused review of the draping process and its impact on the resin infusion in Liquid Composite Molding, Thin-Walled Structures 205 (2024) 112362.

[16] D. Dörr, Simulation of the Thermoforming Process of UD Fiber-Reinforced Thermoplastic Tape Laminates, Dissertation, Karlsruhe, 2019.

[17] D. Soulat, A. Cheruet, P. Boisse, Simulation of continuous fibre reinforced thermoplastic forming using a shell finite element with transverse stress, Computers & Structures 84 (2006) 888–903.

[18] P. Boisse, N. Hamila, E. Vidal-Sallé, F. Dumont, Simulation of wrinkling during textile composite reinforcement forming. Influence of tensile, in-plane shear and bending stiffnesses, Composites Science and Technology 71 (2011) 683–692.

[19] S. Allaoui, P. Boisse, S. Chatel, N. Hamila, G. Hivet, D. Soulat, E. Vidal-Salle, Experimental and numerical analyses of textile reinforcement forming of a tetrahedral shape, Composites Part A: Applied Science and Manufacturing 42 (2011) 612–622.

[20] S. P. Haanappel, R. Thije, U. Sachs, B. Rietman, R. Akkerman, Formability analyses of uni-directional and textile reinforced thermoplastics, Composites Part A: Applied Science and Manufacturing 56 (2014) 80–92.

[21] D. Dörr, F. J. Schirmaier, F. Henning, L. Kärger, A viscoelastic approach for modeling bending behavior in finite element forming simulation of continuously fiber reinforced composites, Composites Part A: Applied Science and Manufacturing 94 (2017) 113–123.

[22] D. Dörr, T. Joppich, D. Kugele, F. Henning, L. Kärger, A coupled thermomechanical approach for finite element forming simulation of continuously fiber-reinforced semi-crystalline thermoplastics, Composites Part A: Applied Science and Manufacturing 125 (2019).

[23] C. Poppe, T. Rosenkranz, D. Dörr, L. Kärger, Comparative experimental and numerical analysis of bending behaviour of dry and low viscous infiltrated woven fabrics, Composites Part A: Applied Science and Manufacturing 124 (2019) 105466.

[24] R. Thije, R. Akkerman, J. Huétink, Large deformation simulation of anisotropic material using an updated Lagrangian finite element method, Computer Methods In Applied Mechanics And Engineering 196 (2007) 3141–3150.

[25] A. A. Skordos, C. Monroy Aceves, M. Sutcliffe, A simplified rate dependent model of forming and wrinkling of pre-impregnated woven composites, Composites Part A: Applied Science and Manufacturing 38 (2007) 1318–1330.

[26] E. Guzman-Maldonado, N. Hamila, N. Naouar, G. Moulin, P. Boisse, Simulation of thermoplastic prepreg thermoforming based on a visco-hyperelastic model and a thermal homogenization, Materials & Design 93 (2016) 431–442.

[27] D. Dörr, F. Henning, L. Kärger, Nonlinear hyperviscoelastic modelling of intra-ply deformation behaviour in Finite element forming simulation of continuously fibre-reinforced thermoplastics, Composites Part A: Applied Science and Manufacturing (2018).

[28] H. Alshahrani, M. Hojjati, Bending behavior of multilayered textile composite prepregs: Experiment and finite element modeling, Materials & Design 124 (2017) 211–224.

28

[29] T. G. Donderwinkel, B. Rietman, S. P. Haanappel, R. Akkerman, Stamp forming optimization for formability and crystallinity, in: AIP Conference Proceedings 1769, 170011, 2016, p. 170029.

[30] G. E. Street, M. S. Johnson, The Intra-Ply Shear Behaviour of Non-Isothermal Thermoplastic Composite Laminates, Journal of Composites Science 7 (2023) 432.

[31] D. Dörr, D. Kugele, T. Joppich, F. Henning, L. Kärger, On the relevance of thermomechanics and crystallization kinetics for FE thermoforming simulation of semi-crystalline thermoplastic tapes, in: Proceedings of the 22nd International ESAFORM Conference on Material Forming: ESAFORM 2019, Vitoria-Gasteiz, Spain, 2019, p. 020011.

[32] N. Bigot, E. Guzman-Maldonado, M. Boutaous, S. Xin, N. Hamila, A Coupled Thermo-mechanical Modelling Strategy Based on Alternating Direction Implicit Formulation for the Simulation of Multilayered CFRTP Thermo-stamping Process, Applied Composite Materials 29 (2022) 2321–2341.

[33] A. Lévy, D. A. Hoang, S. Le Corre, On the Alternate Direction Implicit (ADI) Method for Solving Heat Transfer in Composite Stamping, Materials Sciences and Applications 08 (2017) 37–63.

[34] N. Bigot, N. Hamila, P. Chaudet, S. Xin, M. Boutaous, Modeling and experimental identification of thermo-kinetic and visco-hyperelastic coupling for semicrystalline thermoplastic continuous fiber composites subjected to processing temperatures, Composites Part A: Applied Science and Manufacturing 178 (2024) 107967.

[35] R. P. R. Cardoso, J. W. Yoon, M. Mahardika, S. Choudhry, R. J. Alves de Sousa, R. A. Fontes Valente, Enhanced assumed strain (EAS) and assumed natural strain (ANS) methods for one-point quadrature solid-shell elements, International Journal for Numerical Methods in Engineering 75 (2008) 156–187.

[36] M. Pagani, S. Reese, U. Perego, Computationally efficient explicit nonlinear analyses using reduced integration-based solid-shell finite elements, Computer Methods In Applied Mechanics And Engineering 268 (2014) 141–159.

[37] M. Schwarze, I. N. Vladimirov, S. Reese, Sheet metal forming and springback simulation by means of a new reduced integration solid-shell finite element technology, Computer Methods In Applied Mechanics And Engineering 200 (2011) 454–476.

[38] K. Rah, W. van Paepegem, A. M. Habraken, R. A. Sousa, R. A. F. Valente, Evaluation of different advanced finite element concepts for detailed stress analysis of laminated composite structures, International Journal of Material Forming 2 (2009) 943–947.

[39] M. Schwarze, S. Reese, A reduced integration solid-shell finite element based on the EAS and the ANS concept-Geometrically linear problems, International Journal for Numerical Methods in Engineering 80 (2009) 1322–1355.

[40] M. Schwarze, S. Reese, A reduced integration solid-shell finite element based on the EAS and the ANS concept-Large deformation problems, International Journal for Numerical Methods in Engineering 85 (2011) 289–329.

[41] M. Mostafa, An improved solid-shell element based on ANS and EAS concepts, International Journal for Numerical Methods in Engineering 108 (2016) 1362–1380.

[42] R. Hauptmann, K. Schweizerhof, A systematic development of 'solid-shell' element formulations for linear and non-linear analyses employing only displacement degrees of freedom, International Journal for Numerical Methods in Engineering 42 (1998) 49–69.

[43] R. Hauptmann, K. Schweizerhof, S. Doll, Extension of the 'solid-shell' concept for application to large elastic and large elastoplastic deformations, International Journal for Numerical Methods in Engineering 49 (2000) 1121–1141.

[44] R. Hauptmann, S. Doll, M. Harnau, K. Schweizerhof, 'Solid-shell' elements with linear and quadratic shape functions at large deformations with nearly incompressible materials, Computers & Structures 79 (2001) 1671–1685.

[45] S. Mattern, C. Schmied, K. Schweizerhof, Highly efficient solid and solid-shell finite elements with mixed strain–displacement assumptions specifically set up for explicit dynamic simulations using symbolic programming, Computers & Structures 154 (2015) 210–225.

[46] S. Reese, P. Wriggers, B. D. Reddy, A new locking-free brick element technique for large deformation problems in elasticity, Computers & Structures 75 (2000) 291–304.

[47] S. Reese, A large deformation solid-shell concept based on reduced integration with hourglass stabilization, International Journal for Numerical Methods in Engineering 69 (2007) 1671–1716.

[48] R. J. Alves de Sousa, R. P. R. Cardoso, R. A. Fontes Valente, J.-W. Yoon, J. J. Grácio, R. M. Natal Jorge, A new one-point quadrature enhanced assumed strain (EAS) solid-shell element with multiple integration points along thickness: Part I-geometrically linear applications, International Journal for Numerical Methods in Engineering 62 (2005) 952–977.

[49] R. J. Alves de Sousa, R. P. R. Cardoso, R. A. Fontes Valente, J.-W. Yoon, J. J. Grácio, R. M. Natal Jorge, A new one-point quadrature enhanced assumed strain (EAS) solid-shell element with multiple integration points along thickness—part II: Nonlinear applications, International Journal for Numerical Methods in Engineering 67 (2006) 160–188.

29

[50] Q. Q. Chen, A. Saouab, P. Boisse, C. H. Park, J. Bréard, Woven thermoplastic composite forming simulation with solid-shell element method, International Journal for Simulation and Multidisciplinary Design Optimization 3 (2009) 337–341.

[51] Q. Chen, P. Boisse, C. H. Park, A. Saouab, J. Bréard, Intra/inter-ply shear behaviors of continuous fiber reinforced thermoplastic composites in thermoforming processes, Composite Structures 93 (2011) 1692–1703.

[52] H. Xiong, E. Guzman Maldonado, N. Hamila, P. Boisse, A prismatic solid-shell finite element based on a DKT approach with efficient calculation of through the thickness deformation, Finite Elements in Analysis and Design 151 (2018) 18–33.

[53] H. Xiong, N. Hamila, P. Boisse, Consolidation Modeling during Thermoforming of Thermoplastic Composite Prepregs, Materials (Basel, Switzerland) 12 (2019).

[54] M. Dia, N. Hamila, M. Abbas, A. Gravouil, A nine nodes solid-shell finite element with enhanced pinching stress, Computational Mechanics 65 (2020) 1377–1395.

[55] C. Poppe, F. Albrecht, C. Krauß, L. Kärger, A 3D Modelling Approach for Fluid Progression during Process Simulation of Wet Compression Moulding – Motivation & Approach, Procedia Manufacturing 47 (2020) 85–92.

[56] C. T. Poppe, C. Krauß, F. Albrecht, L. Kärger, A 3D process simulation model for wet compression moulding, Composites Part A: Applied Science and Manufacturing 50 (2021) 106379.

[57] J.-W. Simon, B. Stier, S. Reese, A solid-shell finite element for fibre reinforced composites, PAMM 12 (2012) 329–330.

[58] O. Barfusz, R. Smeenk, S. Reese, Solid-shell formulations based on reduced integration - investigations of anisotropic material behaviour at large deformations, PAMM 18 (2018) 201800078.

[59] B. Schäfer, D. Dörr, L. Kärger, Reduced-Integrated 8-Node Hexahedral Solid-Shell Element for the Macroscopic Forming Simulation of Continuous Fibre-Reinforced Polymers, Procedia Manufacturing 47 (2020) 134–139.

[60] B. Schäfer, D. Dörr, L. Kärger, Potential and challenges of a solid-shell element for the macroscopic forming simulation of engineering textiles, ESAFORM 2021 (2021).

[61] B. Schäfer, J. Mitsch, L. Kärger, 3D solid-shell element for macroscopic composite forming simulation enabling thickness prediction, Composites Part A: Applied Science and Manufacturing (2025) 109162.

[62] J. Mitsch, B. Schäfer, J. P. Wank, L. Kärger, Considering the viscoelastic material behavior in a solid-shell element for thermoforming simulation, in: Material Forming: ESAFORM 2024, Materials Research Forum LLC, 2024, pp. 457–466.

[63] J. Mitsch, B. Schäfer, L. Kärger, Significance of the material parameters within a three-dimensional solid-shell element for thermoforming simulation, in: Materials Research Proceedings, volume 54, Materials Research Forum LLC, 2025, pp. 363–372.

[64] A. J. M. Spencer, Continuum Theory of the Mechanics of Fibre-Reinforced Composites, Springer Vienna, Vienna, 1984.

[65] A. Spencer, Theory of fabric-reinforced viscous fluids, Composites Part A: Applied Science and Manufacturing 31 (2000) 1311–1321.

[66] A. Bertram, Elasticity and Plasticity of Large Deformations, Springer International Publishing, Cham, 2021.

[67] T. Belytschko, W. K. Liu, B. Moran, K. I. Elkhodary, Nonlinear Finite Elements for Continua and Structures, 2. ed., 1. publ. ed., Wiley, Chichester, 2014.

[68] C. W. Macosko, Rheology: Principles, Measurements, and Applications, Advances in Interfacial Engineering Series, Wiley-VCH, New York NY u.a., 1994.

[69] M. A. Valverde, J. P.-H. Belnoue, R. Kupfer, L. F. Kawashita, M. Gude, S. R. Hallett, Compaction behaviour of continuous fibre-reinforced thermoplastic composites under rapid processing conditions, Composites Part A: Applied Science and Manufacturing 149 (2021) 106549.

[70] J. C. Simo, M. S. Rifai, A class of mixed assumed strain methods and the method of incompatible modes, International Journal for Numerical Methods in Engineering 29 (1990) 1595–1638.

[71] J. C. Simo, F. Armero, Geometrically non-linear enhanced strain mixed methods and the method of incompatible modes, International Journal for Numerical Methods in Engineering 33 (1992) 1413–1449.

[72] J. Simo, F. Armero, R. Taylor, Improved versions of assumed enhanced strain tri-linear elements for 3D finite deformation problems, Computer Methods In Applied Mechanics And Engineering 110 (1993) 359–386.

[73] K.-J. Bathe, E. N. Dvorkin, A formulation of general shell elements-the use of mixed interpolation of tensorial components, International Journal for Numerical Methods in Engineering 22 (1986) 697–722.

[74] T. Belytschko, I. Leviathan, Physical stabilization of the 4-node shell element with one point quadrature, Computer Methods in Applied Mechanics and Engineering 113 (1994) 321–350.

[75] P. Betsch, E. Stein, An assumed strain approach avoiding artificial thickness straining for a non-linear 4-node shell element, Communications in Numerical Methods in Engineering 11 (1995) 899–909.

[76] M. Bischoff, E. Ramm, Shear deformable shell elements for large strains and rotations, International Journal for Numerical Methods in Engineering 40 (1997) 4427–4449.

[77] M. Schwarze, I. N. Vladimirov, S. Reese, On the implementation of the EAS and ANS concept into a reduced integration continuum shell element and applications to sheet forming, International Journal of Material Forming 2 (2009) 919–922.

[78] B. B. J. Schäfer, Macroscopic Forming Simulation of Unidirectional Non-Crimp Fabrics: Hyperelastic Material Modeling and 3D-solid-shell Approach, Dissertation, Karlsruher Institut für Technologie (KIT), 2024.

[79] R. H. W. ten Thije, R. Akkerman, Solutions to intra-ply shear locking in finite element analyses of fibre reinforced materials, Composites Part A: Applied Science and Manufacturing 39 (2008) 1167–1176.

[80] N. Hamila, P. Boisse, Locking in simulation of composite reinforcement deformations. Analysis and treatment, Composites Part A: Applied Science and Manufacturing 53 (2013) 109–117.

[81] N. Hamila, P. Boisse, Tension locking in finite-element analyses of textile composite reinforcement deformation, Comptes Rendus Mécanique 341 (2013) 508–519.

[82] A. Rohatgi, WebPlotDigitizer, 2024 [accessed 17.04.25].

[83] M. A. Khan, T. Mabrouki, E. Vidal-Sallé, P. Boisse, Numerical and experimental analyses of woven composite reinforcement forming using a hypoelastic behaviour. Application to the double dome benchmark, Journal of Materials Processing Technology 210 (2010) 378–388.

31

Declaration of interests

☒ The authors declare that they have no known competing financial interests or personal relationships that could have appeared to influence the work reported in this paper.

☐ The authors declare the following financial interests/personal relationships which may be considered as potential competing interests: